Cellular/Molecular

RIM1/2-Mediated Facilitation of Cav1.4 Channel Opening Is Required for Ca^{2+}-Stimulated Release in Mouse Rod Photoreceptors

Chad P. Grabner,[1] Maria A. Gandini,[2] Renata Rehak,[2] Yun Le,[3] Gerald W. Zamponi,[2] and Frank Schmitz[1]

[1]Institute of Anatomy and Cell Biology, Saarland University, Homburg 66421, Germany, [2]Department of Physiology and Pharmacology, Hotchkiss Brain Institute and Alberta Children's Hospital Research Institute, University of Calgary, Calgary, Alberta T2N 1N4, Canada, and [3]Department of Medicine, University of Oklahoma Health Sciences Center, Oklahoma City, Oklahoma 73104-5020

Night blindness can result from impaired photoreceptor function and a subset of cases have been linked to dysfunction of Cav1.4 calcium channels and in turn compromised synaptic transmission. Here, we show that active zone proteins RIM1/2 are important regulators of Cav1.4 channel function in mouse rod photoreceptors and thus synaptic activity. The conditional double knock-out (cdko) of RIM1 and RIM2 from rods starting a few weeks after birth did not change Cav1.4 protein expression at rod ribbon synapses nor was the morphology of the ribbon altered. Heterologous overexpression of RIM2 with Cav1.4 had no significant influence on current density when examined with $BaCl_2$ as the charge carrier. Nonetheless, whole-cell voltage-clamp recordings from cdko rods revealed a profound reduction in Ca^{2+} currents. Concomitantly, we observed a 4-fold reduction in spontaneous miniature release events from the cdko rod terminals and an almost complete absence of evoked responses when monitoring changes in membrane incorporation after strong step depolarizations. Under control conditions, 49 and 83 vesicles were released with 0.2 and 1 s depolarizations, respectively, which is close to the maximal number of vesicles estimated to be docked at the base of the ribbon active zone, but without RIM1/2, only a few vesicles were stimulated for release after a 1 s stimulation. In conclusion, our study shows that RIM1/2 potently enhance the influx of Ca^{2+} into rod terminals through Cav1.4 channels, which is vitally important for the release of vesicles from the rod ribbon.

Key words: CaV1.4; evoked release; mouse rod photoreceptor; night blindness; ribbon synapse; RIM

Significance Statement

Active zone scaffolding proteins are thought to bring multiple components involved in Ca^{2+}-dependent exocytosis into functional interactions. We show that removal of scaffolding proteins RIM1/2 from rod photoreceptor ribbon synapses causes a dramatic loss of Ca^{2+} influx through Cav1.4 channels and a correlated reduction in evoked release, yet the channels remain localized to synaptic ribbons in a normal fashion. Our findings strongly argue that RIM1/2 facilitate Ca^{2+} entry and in turn Ca^{2+} evoked release by modulating Cav1.4 channel openings; however, RIM1/2 are not needed for the retention of Cav1.4 at the synapse. In summary, a key function of RIM1/2 at rod ribbons is to enhance Cav1.4 channel activity, possibly through direct or indirect modulation of the channel.

Introduction

Several visual defects result from the malfunction of photoreceptors. The photo-transduction cascade can be compromised by the expression of faulty signaling components in their outer segments (Makino et al., 2006; Zhang et al., 2007; Nikonov et al., 2008; Toledo et al., 2011) or from loss of external contributions from the pigment epithelium (Grimm et al., 2000; Kiser et al., 2012). In other instances, the photoreceptors maintain normal phototransduction, but they are unable to signal to the inner retina because they form abnormal synaptic connections with bipolar and horizontal cells.

Received Feb. 17, 2015; revised Aug. 17, 2015; accepted Aug. 19, 2015.

Author contributions: C.P.G., G.W.Z., and F.S. designed research; C.P.G., M.A.G., and F.S. performed research; C.P.G., R.R., Y.L., G.W.Z., and F.S. contributed unpublished reagents/analytic tools; C.P.G. and M.A.G. analyzed data; C.P.G., G.W.Z., and F.S. wrote the paper.

F.S. was supported by the Deutsche Forschungsgemeinschaft (Grant SFB894 A7). G.W.Z. is a Canada Research Chair and is supported by grants from the Canadian Institutes for Health Research. M.A.G. is supported by a Conacyt Fellowship. We thank Pascal Kaeser at Harvard Medical School for reading the manuscript and providing helpful comments.

Correspondence should be addressed to Chad P. Grabner, Department of Ophthalmology, Feinberg School of Medicine, Northwestern University, 645 North Michigan Avenue, Suite 440, Chicago, IL 60611. E-mail: chadgrabner@gmail.com.

DOI:10.1523/JNEUROSCI.0658-15.2015

 0270-6474/15/3513133-15$15.00/0

Numerous mutations in the α1F pore-forming subunit of L-type voltage-gated calcium channels (Cav1.4) have been identified in patients with impaired vision (Boycott et al., 2001; McRory et al., 2004; Hoda et al., 2005; Mansergh et al., 2005). These mutations are grouped together and referred to as incomplete congenital stationary night blindness (incomplete CSNB) or type-2 CSNB (Boycott et al., 2001). When electroretinograms (ERGs) are made from these subjects under dim lighting, a functional photo-transduction signal is witnessed (the a-wave is normal), but it is missing a normal BPC response (no b-wave) (Mansergh et al., 2005). Given the selective enrichment of the Cav1.4 subunit at photoreceptor ribbon synapses (Morgans, 2001; Specht et al., 2009; Liu et al., 2013; Zabouri and Haverkamp, 2013) and the fact that there is no known expression in the inner retina, it is assumed that synaptic defects associated with type-2 CSNB result from a reduction in Cav1.4-dependent exocytosis from rods under dim lighting.

Rab interacting molecules (RIMs) are well known to enhance synaptic transmission (Castillo et al., 2002; Schoch et al., 2006), which may depend on their ability to physically associate with Cav channels to organize the presynaptic, active zone architecture (Kaeser et al., 2011; Südhof, 2012). Other groups have stressed that RIMs associate with Cav channels to stabilize their opening (Kiyonaka et al., 2007) and a wide range of Cav channels appear to be influenced by RIMs (for review, see Simms et al., 2014). RIMs were first described at active zones in retinal photoreceptors (Wang et al., 1997) and others have confirmed this finding (tom Dieck et al., 2005; Limbach et al., 2011) and generated very insightful anatomical and molecular routes for vesicle and Cav interactions. Nevertheless, little is known about the functional role of RIMs at ribbon synapses in the retina. To explore whether RIM1/2 influence synaptic processes at rod terminals, we deleted all forms of RIM1/2 from rods and measured Ca^{2+} currents and, for the first time, monitored exocytosis directly from individual mouse rods. The loss of RIM1/2 led to a reduction in calcium current and a concurrent diminution of evoked and unevoked exocytosis, but the expression level of Cav1.4 was normal and ribbons appeared unaltered. The data strongly suggest that RIM1/2 are needed for the proper functioning of Cav1.4 at rod ribbon synapses. We propose that the combination of Cav1.4 and RIM1/2 at the ribbon creates a functional active zone that enables rods to respond to a depolarizing voltage signal at lights off with a rapid secretory response.

Materials and Methods

Animal handling. Mice were maintained on a 12 h daylight cycle and housed according to Saarland University Institutional Animal Care and Use Committee guidelines. The LMOP-Cre line has been described previously by Le et al., 2006 and the animals were kindly provided by Christian Grimm (Zurich University, Zürich, Switzerland). LMOP-Cre hemizygotic mice were crossed with wild-type C57BL/J6 partners. Mice engineered with floxed *RIM1ff* and *RIM2ff* genes have been described previously (Kaeser et al., 2008; Kaeser et al., 2011) and were kindly provided by Thomas Südhof and Pascal Kaeser (Stanford University, Stanford, CA). To generate the conditional photoreceptor-specific knock-outs of RIM1/2, *LMOP-Cre* mice were crossed into the purely homozygous floxed *Rim1/2* line (*RIM1ff/2ff* line). Only one parent was *LMOPcre*$^+$ in an effort to minimize the number of *cre* transgene copies. Each litter generated between 30% and 70% *cre*$^+$ offspring and the mice without *cre* were used as control littermates. Both male and female mice were used for experiments.

Isolation of eyes. Mice were deeply anesthetized in a chamber pre-equilibrated with isoflurane, which rendered them unresponsive to tail and paw pinch within 1 min. The anesthetized animal was immediately killed by cervical dislocation. Intact eyes were removed and then bathed in physiological saline for further dissection, or frozen for cryosectioning (see below).

Anti-Cav1.4 antibodies. Three antibodies targeting the C-terminal portion of the Cav1.4 subunit were used for Western blotting and/or immunofluorescence (IF). The anti-Cav1.4-human, rabbit polyclonal antibody has been described previously (McRory et al., 2004; Doering et al., 2008). Briefly, this antibody was generated against a 65 fragment peptide (aa 1658–1723) from human Cav1.4 [National Center for Biotechnology Information (NCBI) sequence ID #NP_005174.2]. A sequence alignment over this same region of human Cav1.4 (aa 1658–1723, NCBI sequence ID #NP_005174.2) and mouse Cav1.4 (aa 1660–1741; NCBI sequence ID #NP_062528.2) reveals that 42 aa residues in the mouse sequence are identical to residues in the immunizing fragment (42/65 or ~65% identity) and a stretch of 22 residues in the human sequence is conserved over 20 residues of the mouse sequence (>90% conserved). This same region is not at all present in Cav1.2 and Cav1.3 of the mouse. A second antibody, referred to as anti-Cav1.4-mouse, was raised against the last 260 aa (aa 1725–1984) of the mouse Cav1.4 sequence (NCBI sequence ID #NP_062528.2). The mouse Cav1.4 immunizing element was prepared as a GST fusion protein and delivered to rabbits. A third antibody, referred to as Cav1.4-CT peptide, was raised in rabbit against a synthetic peptide consisting of the final 18 residues of Cav1.4 (SRFDEEDLGDEMACVHAL-C-terminus) that overlaps with the end of the larger Cav1.4-mouse antigen. Both the anti-Cav1.4-mouse and anti-Cav1.4-CT peptide rabbit antibodies were affinity purified by absorbing and eluting them from the antigen GST-Cav1.4-mouse fusion protein that had been electrotransferred to nitrocellulose (Olmsted, 1981). The control staining was made with the affinity purification's unbound serum fraction, which did not bind to immobilized GST-Cav1.4-mouse and, when used for IF, did not generate staining in the retina. This is in contrast to the purified "bound" antibody fraction that gave strong ribbon staining at rod ribbons, as illustrated in Figures 3 and 7. Additional anti-α1-subunit antibodies were purchased from Alomone, Cav1.2 (ACC-003), Cav1.3 (ACC-005), and a broad spectrum α1Pan (ACC-004) that is directed for a 19 aa stretch common to Cav1 (α1C,D,F,S) and Cav2 (α1A,B,E).

Other antibodies. Other antibodies used were as follows: anti-RIM2, rabbit polyclonal (Synaptic Systems, 140–303); anti-RIM1, rabbit polyclonal (Synaptic Systems, 140–003) and anti-RIM1 mouse monoclonal (BD Transduction Laboratories, 610907); anti-Fodrin/α-spectrin, clone AA6, mouse monoclonal (ICN Biomedicals); lectin PNA-Alexa Fluor 568 (Invitrogen, L32458): anti-Ribeye/U2656 rabbit polyclonal antibody (Schmitz et al., 2000); anti-CtBP2 mouse monoclonal (BD Transduction Laboratories, 612044); anti-Cre Recombinase, rabbit polyclonal (Novagen, 69050); and anti-Cre recombinase, mouse monoclonal (Covance, MMS-106P). The anti-Syt1 mouse monoclonal antibody mAb48 developed by L. Reichardt was obtained from the Developmental Studies Hybridoma Bank/ National Institute of Child Health and Human Development at The University of Iowa.

Immunostaining of cryosections. Freshly isolated eyes (see above) were flash frozen in isopentane cooled on liquid nitrogen. Eyes were stored in liquid nitrogen or kept at −80°C until the time of mounting for sectioning. Frozen eyes were mounted in Tissue-Tek optimal cutting temperature medium (VWR International) at −20°C and cut at 10- to 15-μm-thick sections, collected on glass slides, immediately heat fixed at 50°C for >10 min, and finally stored at −20°C. Control and experimental samples were sectioned during the same session and, in most instances, samples from 3–6 different littermates were mounted in a single block and sectioned together.

For experiments that required staining of Cre, the sections had to be fixed with paraformaldehyde (PFA) to prevent washout of Cre, but the use of standard PFA fixation negatively affected antibodies used for Cav staining; therefore, we optimized a protocol for costaining Cre and Cav channels. First, the PFA was freshly depolymerized at ~70°C in PBS, pH 7.4, filtered, and cooled on ice. Second, cryosections that had been stored at −20°C were transferred to ice-chilled 3% PFA for 20 s. Next, the sections were washed in PBS, blocked in 1% bovine serum albumin (BSA) at room temperature, and then permeabilized in 0.3% Triton

X-100 plus 1% BSA in PBS, pH 7.4 (BSA-Triton). The sections were incubated for 16 h at 4°C in the primary antibodies (prepared in BSA-Triton). After washing, the secondary antibody was added at a dilution of 1:1000 in 1% BSA, PBS for 1 h at room temperature. Two primary antibodies were added simultaneously over the first night (one rabbit IgG, anti-Cav, and the other mouse IgG, anti-Cre) and then anti-CtBP2 was added for the second overnight incubation. In most instances, rabbit IgGs were labeled with chicken anti-rabbit IgG-Alexa Fluor 488 (Invitrogen, A21441) and mouse IgGs were labeled with goat anti-mouse IgG-Alexa Fluor 647 (Invitrogen, A21245).

Confocal images of immunolabeled samples were collected as a stack of optical sections through the entire ~10 μm cryosections and the images are presented here as maximal projections using ImageJ software. To determine the "contour length" of the ribbon, optical sections were inspected in upper regions of the outer plexiform layer (OPL) containing rod terminals, away from the PNA-labeled cone terminals. Ribbon profiles that were captured in the plane of a 1 μm optical section typically appearing as U-shaped structures offer the most complete contour of a ribbon. Ribbons running perpendicular or tangential to the optical sections were observed in multiple sections and are not included in the analysis. The contour length was measured by drawing a segmented line starting at one end of the ribbon, tracing along its central ridge until reaching the other end of the ribbon. Contour lengths ranged from 1.2 to 1.9 μm (see Results). The contour is not the same as the side-to-side width of the ribbon, which is typically ~1 μm. Sections were collected with a calibrated pixel resolution of 0.02 or 0.04 μm and these values were used to set the scale in ImageJ.

Immunostaining of 0.5-μm-thick resin sections for obtaining high-resolution images was performed as described previously (Wahl et al., 2013; Dembla et al., 2014) and used only in Figure 7, *I* and *J*.

Western analysis. Freshly isolated eyes were dissected in ice-chilled, ~4°C mouse extracellular solution (MES) with Ca^{2+} reduced to 0.5 mM (see below). The entire neural retina was carefully separated from the pigment epithelium, vitreous, and optic nerve. Each retina was homogenized in 160 μl of a standard SDS-loading buffer to generate a total lysate, which was heated to 95°C for 10 min and loaded directly onto PAGE gels or stored at −20°C. To better resolve the Cav channels, individual retinas were prepared in the following detergent-rich buffer to yield a membrane-enriched fraction containing the following (in mM): 150 NaCl, 10 Tris, 0.1% SDS, 0.5% sodium cholate, 1% NP-40, 0.1% PMSF, and one protease inhibitor mixture tablet per 10 mls (Complete Ultra EDTA-Free Tablets, Roche), pH 7.4. Triturated retinas were incubated for 1 h on ice with agitation and then centrifuged at 16,000 × *g* for 20 min at 4°C, which yielded a soft sediment that was separated from the supernatant (Fig. 3*I* illustrates the partition of membrane proteins into the supernatant). The samples were frozen in liquid nitrogen and stored at −80°C. Figure 3*I* shows a Western blot that compares the supernatant and pellet fractions derived from the Cav extraction procedure described here and the supernatant fraction contains the Cav and synaptic proteins, whereas the pellet fraction is protein poor.

Western samples were separated by SDS-PAGE using a 4% acrylamide stacker and a discontinuous running gel of two parts, with 6% acrylamide (~4 cm length) on top and 10% acrylamide (2 cm length) on bottom (Fig. 1*B* illustrates the range of proteins resolved within a gel, from Cre at 39 kDa to Fordrin at 250 kDa). When probing for Cav channels using membrane-enriched lysates, 12% of a retina was loaded per lane. In contrast, synaptic proteins processed from total lysates (in SDS loading buffer) required only 3–5% of a retina per lane. Samples were electrotransferred onto nitrocellulose membranes, washed in PBS, and then blocked in 2% BSA/PBS, pH 7.3, for 1 h. Primary antibodies were diluted in the blocking buffer plus 0.1% azide and incubated with membranes for 16–24 h. The following HRP-conjugated secondary antibodies were used at a dilution of 1:10,000: goat anti-rabbit (Sigma-Aldrich, A6154) and goat anti-mouse (Sigma-Aldrich, A3673) and membranes were incubated with the secondary antibodies for >1 h in the absence of azide. Blots were developed with enhanced chemiluminescence reagents and imaged over time with digital camera driven by Quantity One software (Bio-Rad).

Quantitation of Western blots. The discontinuous SDS-PAGE with 6% and 10% acrylamide (see Figs. 1, 2, 3, and 7) captured the following large proteins in the 6% acrylamide portion: Fodrin ~250 kDa; Cav channels, 130–250 kDa; long forms of Rim1/2, ~160–220 kDa; and Ribeye, ~115 kDa detected with anti-CtBP2 or U2656. The lower 10% acrylamide portion of the gel resolved the following proteins under ~70 kDa: Synatotagmin-1 (Syt1), ~65 kDa, CtBP2 transcription factor, ~45 kDa, and Cre, ~39 kDa. Cre protein expression was always examined for each animal and routinely verified per gel lane with accompanying probes at higher MWs. The control and cre^+ littermate samples were placed in neighboring lanes and multiples from each group were simultaneously compared. Densitometry measurements were made with the plugin in ImageJ using rectangular boxes of fixed areas and placing them around each lane, with sufficient baseline above and below the bands of interest. Background offsets were subtracted from each band to attain the absolute intensities. Relative intensities were determined per Western blot by normalizing the maximal signal to 1 and other lanes within the gel were expressed as a fraction of the maximum. Statistics are reported as mean ± SE (mean/SE), and the *p* value was measured with the unpaired Student's *t* test (OriginLab software; MicroCal).

Electrophysiology. Dissections were performed in chilled ~8°C, low Ca^{2+} MES containing the following (in mM): 135 NaCl, 2.5 KCl, 0.5 $CaCl_2$, 1 $MgCl_2$ hexahydrate, 10 glucose, and 15 HEPES, pH 7.35. After separating the neural retina from the pigment epithelium and removing the vitreous, retinas were mounted vitrea side down on nitrocellulose membrane and stored at 12°C in an aerated refrigerator until slicing. Tissue was kept ~6 h maximum, with most measurements made within the first 2 h after the animal was killed. Slices were made with a two-sided razor blade, sectioned to ~100- to 200-μm-thick slices, and visualized in cross-section with differential interference optics equipped with a high-resolution, 1.2 numerical aperture, 60× water-immersion objective, and a final 2× magnifying lens in front of the camera.

Electrophysiological measurements were made with a HEKA EPC-10, dual head-stages, and equipped with HEKA's Patchmaster software. Whole-cell electrodes were fabricated from thick-wall, standard glass capillary tubes and the tip region was coated with dental wax. Pipette resistance was ~8.5 MΩ with the standard MES bath solution and either of the intracellular solutions. The following two intracellular solutions with high Ca^{2+} chelator concentrations were used to measure calcium currents (I_{Ca}) (containing the following in mM): 105 $CsCH_3SO_4$, 20 TEA-Cl, 2 $MgCl_2$ hexahydrate, 3 MgATP, 0.2 NaGTP, 10 HEPES, and 10 EGTA, along with 0.1 mg/ml Lucifer yellow (LY), pH adjusted to 7.30 with CsOH to an osmolarity of 295; or alternatively, 5 mM BAPTA replaced EGTA. The Ca^{2+} chelators were needed to block the Ca^{2+}- activated chloride channels (Bader et al., 1982) and the Ca^{2+}- activated potassium channels (Big-K^+), as well as secretion-activated glutamate currents (Szmajda and Devries, 2011) and inhibitory proton feedback (DeVries, 2001). Series resistance in whole-cell, voltage-clamp conditions was ~20 MΩ and access was gained via suction. To characterize the behavior of the small synaptic events, some of the measurements were made with thiocyanate in the intracellular solution, replacing $CH_3SO_4^-$ and Cl^-, to determine whether thiocyanate promoted larger glutamate transporter currents.

The standard protocol for monitoring I_{Ca} or membrane capacitance required an exchange of extra-cellular solutions to minimize interfering conductances. First, the tissue was equilibrated for ~15 min in a perfusion, recording chamber with standard MES containing 2 mM $CaCl_2$ at a room temperature of 28°C. Second, rod somata near the OPL were identified for whole-cell patch clamp. The cells were infused with the intracellular solution for >2 min before being depolarized. During this rest period, the extracellular media was exchanged to TEA-Cs MES (mM): 105 NaCl, 2.5 KCl, 25 TEA-Cl, 5 CsCl, 2 $CaCl_2$, 1 $MgCl_2$ hexahydrate, 10 glucose, and 15 HEPES, pH 7.35. Cesium in the extracellular solution blocked the I_h current in the terminal (Cs inside is not sufficient for this purpose; Bader et al., 1982) and TEA outside reduced outward currents common to the inner and outer segments. Continuous traces were collected at rest to assess whether the cell was generating miniature events that represent secreted glutamate feedback onto the terminal, which indicates that a terminal is present (see Fig. 5).

To attain a current–voltage (*I–V*) relationship for the Cav channels using a ramp protocol, all ramps started at −80 mV and stepped down to

−100 mV for 500 ms to verify that I_h was absent, and then the cells where depolarized at a rate of 1 V/s or 0.2 V/s from −100 to +40 mV. Ramps were repeated every ~20 s starting ~2 min after entry. Once stable ramps were acquired, typically after 4 min from the start of whole-cell entry, I_{Ca} was blocked by switching the extracellular solution to a Ca^{2+}-free MES containing 4 mM $CoCl_2$. The voltage ramp responses were analyzed by taking the linear portion of the current from −80 to −60 mV and subtracting it from the entire trace. A Boltzmann function was used to fit the *I–V* ramps to attain the maximum inward calcium current and $V_{m1/2}$.

Recordings were made from rod somata near the OPL and often the ribbon was contained in the soma; alternatively, the somata were set apart from the OPL by ~1 row creating a short axon of ~5–8 μm in length to the small terminal, which was documented after the recording by filling of the cell with the intracellular tracer LY (see Figs. 4*A*,*B*, 5*A*,*B*). A total of 56% of controls and 62% of conditional double knockout (cdko) rods had short axons connecting the terminal and the remaining recordings without a connecting axon were made at the OPL. In instances with no measureable I_{Ca}, a terminal or synaptic miniature events had to be observed for the cell to be included in the study of I_{Ca}. An indicator of the small size of the rods is their whole-cell membrane capacitance (C_m), which ranged from 0.8 to 2 pF. The soma alone at OPL showed <1 pF, whereas more intact rods had C_m values of ~2 pF. These values are similar to what is predicted from published results derived from preparations other than mouse rods. For example, dissociated goldfish bipolar cell terminals are semispherical, range from 10 to 15 μm, and have C_m values between 2 and 4 pF (Mennerick et al., 1997); mouse rod somata are ~5–7 μm in diameter and have a C_m of ~1 pF.

Post hoc verification of Cre^+ cells required documenting cell location and then staining for Cre. After the recording, the location and distance of the tracer-filled cell relative to the end of the slice was documented and then the slice was removed from the recording chamber and placed in 3% PFA/PBS at pH 7.4 for 30–60 min. After washing the tissue in PBS, the slice was permeabilized in 1% Triton, 3% BSA/PBS at pH 7.4 at room temperature for 20 min and then incubated overnight with the rabbit polyclonal anti-Cre antibody (from Novagen; see above) with 0.3% Triton, 1% BSA/PBS at pH 7.4. The next day, the secondary anti-rabbit Alexa Fluor 568 was used to visualize Cre indirectly. Sections were viewed in the same orientation as the original recording configuration and the cell's location was found by first dialing back the distance from the end of the slice and then inspecting this area for the LY fluorescently labeled cell. If the nucleus was pulled out of the soma when the electrode was retracted, then LY retention in the remaining portions of the LY-labeled cell were examined for Cre. The inner segment/ellipsoid region where Cre protein is synthesized has the highest levels of Cre staining (see Fig. 4*B*) and the axon terminals were also Cre^+ but less intensely. In addition, bright-field images were taken to orient the OPL and outer nuclear layer (ONL) images from postrecording and poststaining as presented in Figures 4 and 6. The pattern of Cre in LMOP mice has a columnar pattern and ~50% of the cells are Cre^+ (Le et al., 2006). In our study, 50% of the recordings that were made from LMOP*cre*$^+$ mice stained positive for Cre.

Analysis of synaptic events. Membrane current traces collected over the first 4 min after cell rupture were analyzed after filtering at 300 Hz. The procedure for aligning and averaging events with Synaptosoft software has been described previously (Grabner et al., 2005). All drugs used to characterize the miniature events were purchased from Tocris Bioscience and delivered at concentrations stated in the Results section.

Membrane capacitance measurements. Recordings were made with HEKA's PatchMaster software using the "sine+dc" Lockin routine. The cell's voltage was held at −80 mV and the stimulating sine wave was applied at 500 Hz, with a 10 mV sine wave amplitude that was sampled at 10 kHz. To ensure the best possible electrical control and the most rapid infusion of the rod terminal, rod somata near the OPL were targeted as described above. To promote release, the intracellular EGTA was lowered to 2 mM EGTA. Membrane currents (I_m) were leak subtracted, as shown in Figure 6, *E* and *F*, and the protocol consisted of an average of four steps from −70 to −62 mV, a portion of the IV that is linear with TEA and Cs^+ in the extracellular solution. The stimulation protocols for estimating evoked C_m began with a 1 s sine wave sweep around −80 mV to determine the C_m baseline, and the next sweep included the depolarization which started with a 0.25 or 1 s sine wave at −80 mV that was then paused for the duration of stimulation and resumed for 1 s after the stimulus. The depolarizing steps were to −25 and −5 mV and durations of 0.2 or 1 s. The change in C_m was measured by setting the prestimulation C_m to zero (baseline) and a linear fit from 0.75–1 s over the poststimulation C_m was made and averaged to generate the change in C_m (see Fig. 6*H*). Over this later stage of postdepolarization, the membrane conductance (G_m) had settled to prestimulus values. Finally, in no instance was a recording with a change in series conductance (G_s) used in the analysis.

Current density measurements from Cav1.4 in cultured cells. Human embryonic kidney tsA-201 cells were cultured and transfected using the calcium phosphate method. Cav1.4 α1F subunit (6 μg), Cavβ_{2a} (6 μg), and Cav$\alpha_2\delta$-1 (6 μg) were cotransfected in absence or presence of RIM2α. In addition, 0.45 μg of a plasmid cDNA encoding the green fluorescent protein was added to the transfection mixture to identify and select transfected cells. Electrophysiological recordings were performed in whole-cell configuration 72 h after transfection at room temperature (22–24°C). The external recording solution contained the following (in mM): 114 CsCl, 20 BaC_{l2}, 1 $MgCl_2$, 10 HEPES, and 10 glucose adjusted to pH 7.4 with CsOH. Pipettes were filled with a solution containing the following (in mM): 108 $CsCH_3SO_3$, 4 $MgCl_2$, 9 EGTA, 9 HEPES, 2 ATP, and 0.6 GTP adjusted to pH 7.2 with CsOH.

Currents were recorded using an Axopatch 220B amplifier (Molecular Devices) by applying 250 ms pulses between −60 and 40 mV in 5 mV increments from a holding potential (V_h) of −100 mV. *I–V* relationships were generated from the peak current obtained during the pulses. All experimental values are given as means ± SE. The *I–V* relationships were fitted with a Boltzmann equation of the form: $I = G_{max} * (V_m - V_r)/(1 + \exp(-(V_m - V_{1/2})/k))$, where *I* is the peak current, V_m is the membrane voltage, $V_{1/2}$ is the voltage for half activation, V_r is the reversal potential, and *k* is the slope factor.

Electron microscopy. For electron microscopy (EM), eyes of light-adapted mice were harvested as described above and dissected to yield eye cups that were fixed and embedded in Epon as described previously (Schoch et al., 2006). Only vesicles attached to the ribbon were analyzed. Analysis of vesicle diameter has also been described previously (Grabner and Zenisek, 2013).

Estimating the number of vesicles released and the number of vesicles on a ribbon. To calculate the capacitance per vesicle, we compared our EM results with that of vesicle profiles measured from hair cells and individual vesicle capacitance measurements measured within the same study (Neef et al., 2007), which reported a mean SV diameter of 37 nm and a capacitance of 45 aF per vesicle. We estimate that our average 32.5 nm vesicle diameter amounted to 34.7 aF. To relate the number of fusing vesicles to the potential number of vesicles tethered to a ribbon, an upper limit of vesicle numbers was estimated by assuming a maximal hexagonal packing of vesicles in a single layer on each side of the ribbon. If vesicles are uniformly sized and their centers are linearly aligned along the length of the ribbon and each vesicle is touching its neighbor, their center-to-center (CTC) distance is ~35 nm (~vesicle diameter) and the number of vesicles per row is simply the length of the ribbon divided by 35 nm; therefore, a contour length of 1.5 μm amounts to 43 SVs per row. If the next row of vesicles are also linearly arranged with a CTC spacing of 35 nm and are touching the rows above and below with CTC distances of 35 nm, but their centers are shifted to an angel of 60° from the row above and below, then they are hexagonally packed and the vertical displacement is less than the CTC distance. The vertical spacing between rows is calculated as Sin(60°) = opposite side/ hypotenuse = (vertical spacing)/(CTC distance of 35 nm), which when rearranged yields a vertical spacing of ~30 nm. Therefore, a ribbon with a height of 300 nm is divided by 30 nm to give 10 rows of SVs. The total number of rows is 10 on each side of the ribbon and 43 vesicles/row: 2 sides × 10 rows × 43 vesicles/row = 860 per ribbon as a maximal estimate.

Results

Targeted knock-out of RIM1/2 from rod photoreceptors

The family of RIM proteins are grouped into long (RIM1α/β and 2α/β) and short forms (2γ, 3γ and 4γ) (Wang and Südhof, 2003).

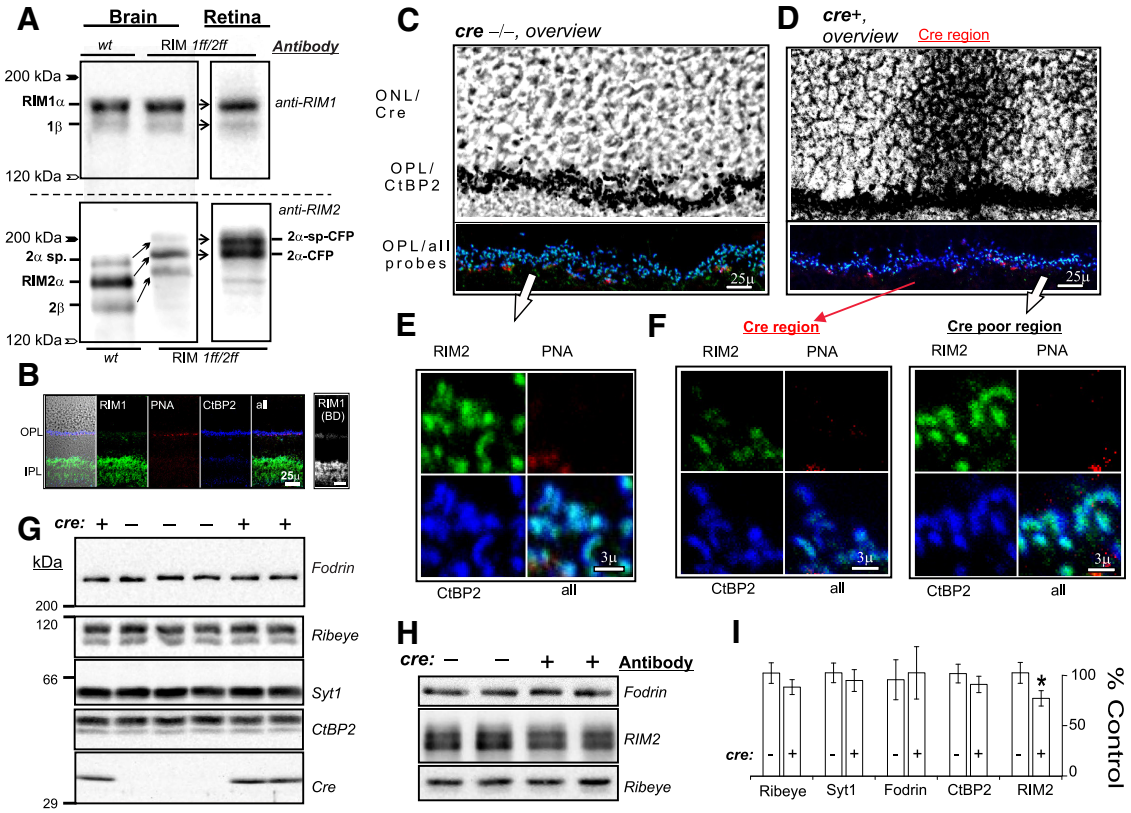

Figure 1. Conditional knock-out of RIM2 in rod photoreceptors is under way as early as 3 weeks of age. ***A***, Forms of RIM1 and RIM2 found in the brain and retina of wild-type and transgenic *RIM1ff/2ff* mice. Expression of RIM $1\alpha \gg 1\beta$ in the retina, which is similar to the proportions in whole-brain lysates (probed with Ms monoclonal anti-RIM1). The floxed *RIM2ff* gene was engineered such that a cyan fluorescent protein was placed at the C-terminal of RIM2 (Kaeser et al., 2011) and therefore all of the RIM2 in the transgenic animal is RIM2-cfp, which is revealed as an upward shift in its migration compared with brain lysates from wild-type animals (the cfp tag is nonfluorescent in the retina). Relative RIM2 expression levels in the brain are RIM $2\alpha > 2\beta \sim 2\alpha$-splice variants ($\alpha$-sp.) and, in the retina, 2α and 2α-sp are equally expressed, but 2β is not detected. The regional distribution of RIM1/2 was examined by immunostaining cryosections of retina ~10 μm thick (***B***–***F***). ***B***, Expression of RIM1 is largely confined to the IPL and this is demonstrated with a rabbit polyclonal anti-RIM1 from Synaptic Systems (left) and a mouse monoclonal against RIM1 from BD Transduction Laboratories (right). Scale bar, 25 μm. ***C***, ***D***, Top overview panels in black and white are composites of transmitted light and fluorescent signals from anti-CtBP2 and anti-Cre immunolabeling (both are Ms monoclonal antibodies and visualized with anti-Ms IgG-Alexa Fluor 648; see Materials and Methods). The transmitted light images outline the ONL and anti-CtBP2 stains Ribeye/ribbons (Schmitz et al., 2000), demarcating the OPL. The section in ***D*** is from a *LMOPcre*$^{+}$ transgenic animal, which shows an intensely stained patch of Cre in the ONL that is designated as a Cre region (samples in ***C*** and ***D*** are from *RIM1ff/2ff* littermates, 3 weeks of age). Bottom overview cropped to the *OPL* is labeled "all probes" because the signals are derived from anti-RIM2 staining (rabbit polyclonal, Alexa Fluor488, shown in green), the cone marker PNA (linked to Alexa Fluor 568, shown in red), and anti-CtBP2 (Ms monoclonal, Alexa Fluor 648, shown in blue). ***E***, ***F***, Regions selected for presentation at higher resolution. The control condition presented in ***C*** and ***E*** and the "Cre-poor region" in ***F*** show that the RIM2 signal overlaps extensively with CtBP2/Ribeye (aqua). The "Cre-rich region" in ***F*** reveals a drop in RIM2 staining. ***G***, ***H***, Present Western blots that were used to compare the synaptic protein levels from anticontrol and transgenic retinas. Individual blots were probed for multiple antigens. The antibodies used are listed on the right side of the blot and the position of the molecular weight standards are on the left (genotype is indicated above each lane). Fodrin was used as a postsynaptic marker (~250 kDa; Schmitz, 2001), and Ribeye (~110 kDa; Schmitz et al., 2000) and Synaptotagmin1 (Syt1, ~60 kDa) were used as presynaptic markers, whereas CtBP2 (~45 kDa) in the context of Western analysis represents the transcription factor that is expressed throughout the retina. ***I***, Graphical summary of the densitometry measurements from Western analysis. Only RIM2 was reduced (see text for values) and no apparent change in the intensity of the synaptic markers was witnessed at 3 weeks. Data are presented as mean ± SE.

The prominent isoforms of RIM1 and 2 expressed in the retina show overlap with those found in whole brain lysates (Fig. 1*A*), but two exceptions exist. The RIM2β isoform is not detected at appreciable levels in retinal lysates, and the larger 2α-splice variant(s) are expressed at relatively higher levels in the retina than brain, with 2α and 2α-splice variants expressed at equal levels (Fig. 1*A*). The distribution of RIM1 in the retina is segregated to the synapses in the inner plexiform layer (IPL) and relatively less staining is observed in the OPL, where photoreceptor terminals are located (Fig. 1*B*). In contrast, RIM2 staining is very intense at rod terminals (Fig. 1*C*–*E*) and widely distributed across the IPL (Regus-Leidig et al., 2010; Limbach et al., 2011).

Deletion of the long forms of RIM1/2 has been achieved with the development of transgenic mice that carry floxed *RIM1* and *RIM2* genes (*RIM1ff/2ff*) (Kaeser et al., 2011). To remove RIM1/2 selectively from rods, mice engineered with the *Long Mouse Opsin Promoter* (*LMOP*)*cre* transgene (Le et al., 2006) were crossed into the *RIM1ff/2ff* line to create cdko mice. The LMOP*Cre* mice produce Cre only in rods, which begins at ~7 d after birth, a few days after ribbon development is initiated (Le et al., 2006). We made the RIM1/2 dko because previous studies have reported that the long forms of RIM1/2 may compensate for one another in certain brain regions, but the dko newborns are not viable (Schoch et al., 2006). To circumnavigate this shortcoming, we developed a rod-specific cdko line.

Figure 1*D* shows the regional expression of Cre in rods of a 3-week-old cdko retina. The synaptic ribbons residing in Cre-rich areas have reduced RIM2 staining, whereas Cre-poor regions in the same field of view reveal higher RIM2 staining (Fig. 1*F*). A significant reduction in RIM2 was also detected with Western analysis when using whole retina lysates from 3-week-old cdko animals (control vs cdko: 1 ± 0.05 and 0.82 ± 0.05, normalized

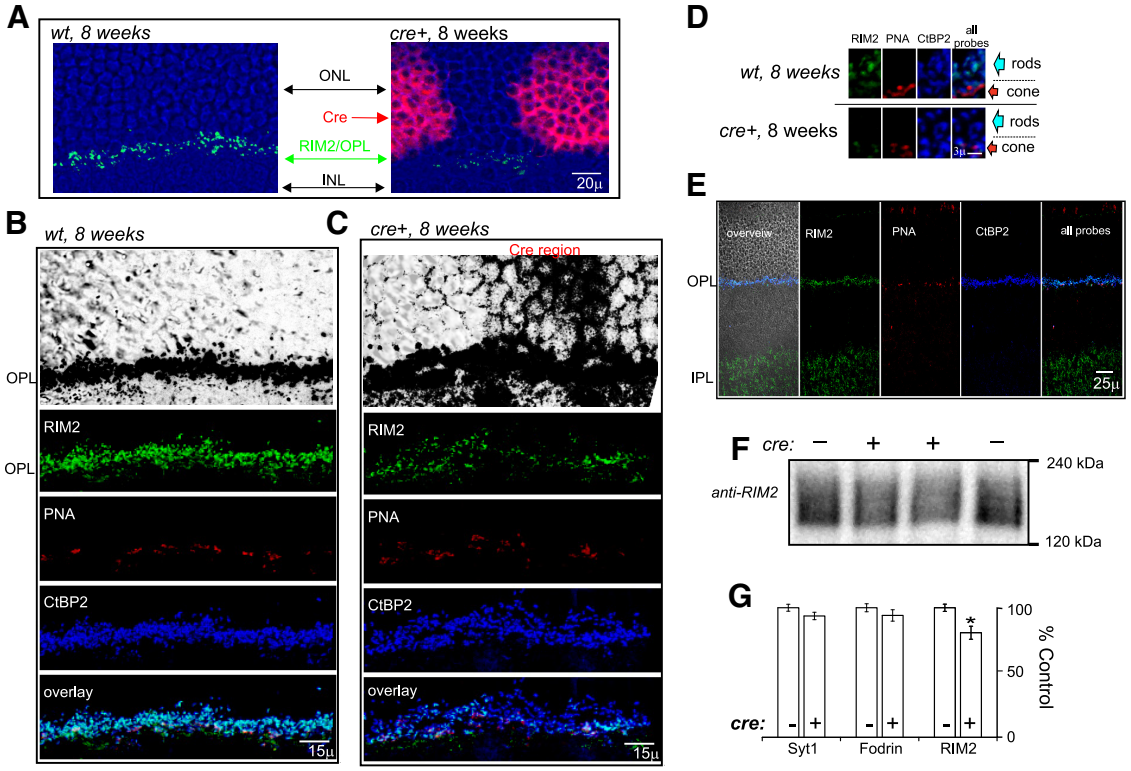

Figure 2. RIM2 is selectively removed from rods expressing Cre by 8 weeks and persists at cone terminals. ***A***, Colabeling of cryosections from 8-week-old littermates. The retinal section from a control (*RIM1ff/2ff*) on the left has a continuous line of RIM2 staining across the OPL (shown in green, and transmitted light is overlaid in blue to demarcate the ONL's rod somata); in contrast, the section from the cdko animal presented on the right has two regions of Cre staining (pink) and the underlying OPL lacks significant RIM2. ***B–D***, Additional probes were used to demonstrate the absence of RIM2 at rod ribbons in regions enriched with Cre, and the constancy of RIM2 at cone terminals. ***B***, ***C***, Top, black and white images are composites of transmitted light and fluorescent signals from anti-CtBP2 and anti-Cre immunolabeling (both are Ms monoclonal antibodies and visualized with anti-Ms IgG-Alexa Fluor 648; see Materials and Methods). The transmitted light images outline the ONL and anti-CtBP2 stains Ribeye/ribbons demarcates the OPL. The lower color images in ***B*** and ***C*** show immunostaining for the antigens indicated (anti-RIM2, rabbit polyclonal, Alexa Fluor 488, shown in green; the cone marker PNA linked to Alexa Fluor 568, shown in red; and anti-CtBP2, Ms monoclonal, Alexa Fluor 648, shown in blue), and the overlay of the various probes are presented in the bottom panels. The control in ***B*** exhibits a continuous band of RIM2 labeling in the OPL, whereas the *cdko* retina shown in ***C*** expresses a patch of Cre that is accompanied by a significant disruption in RIM2 in the underlying OPL. ***D***, RIM2 staining that remains in Cre regions is localized to "cone terminals" that are labeled with PNA and occupy the innermost aspects of the OPL. The regions where the rod terminals are located are indicated with turquoise arrowheads. The control exhibits RIM2, which is seen to colocalize with CtBP2 in the overlay. In contrast, RIM2-free rod ribbons are seen in the Cre $^{+}$ region, yet the underlying cone expresses RIM2, which is a consequence of the cones not expressing Cre. ***E***, RIM2 is heavily expressed in the OPL and a major portion of RIM2 is expressed in the IPL. ***F***, Example of a Western blot showing the decreased levels of RIM2 in cdko animals (3 months of age). ***G***, Summary plots of RIM2 and other synaptic protein levels found in retinas of 3-month-old mice. Data are presented as mean ± SE.

mean ± SE; $p = 0.008$; $n = 6$ control and 7 cdko mice), whereas expression levels of other synaptic markers from cdko mice were normal at 3 weeks after birth (control vs Cre; Fodrin: 0.93 ± 0.19 vs 1 ± 0.25, $p = 0.72$; Ribeye: 1 ± 0.10 vs 0.86 ± 0.07, $p = 0.26$; Syt1: 1 ± 0.09 vs 0.89 ± 0.08, $p = 0.28$; CtBP2: 1 ± 0.09 vs 0.89 ± 0.09, $p = 0.40$; $n = 6$ control and 7 cdko mice; Fig. 1*G–I*). The immunofluorescence results at 8 weeks show RIM2 missing from patches of retina with Cre expression (Fig. 2*A–D*) and, in the same field of view, only cone terminals, which do not express Cre, show RIM2 labeling (Fig. 2*D*). Western blots of retinal lysates from older cdko mice, 3–9 months of age (Fig. 2*F*), showed a 19% reduction in RIM2 compared with their respective controls (control vs cdko: 1 ± 0.03 vs 0.81 ± 0.04; $p = 0.0006$, $n = 10$ and 18), whereas other synaptic markers were expressed at control levels (control vs cdko; Fodrin: 1 ± 0.03 vs 0.94 ± 0.04, $p = 0.27$ from $n = 18$ and 15; Syt1: 1 ± 0.03 and 0.94 ± 0.03, $p = 0.12$; from $n = 19$ and 16 mice; Fig. 2*G*). Considering that a major portion of RIM2 is expressed in the inner retina (Fig. 2*E*) and only 50% of the photoreceptors express Cre (Le et al., 2006), the reduction in RIM2 observed on aggregate (Western analysis) indicates a dramatic drop in RIM2 expression in the Cre-targeted rods and the immunofluorescence results reveal a focal depletion of RIM2 from rods in Cre regions and a persistence of RIM2 only in cones that do not express Cre (Fig. 2*D*).

Cav1.4 L-type channels are highly expressed at photoreceptor ribbons

The type of Cav channel operating at rod ribbons are believed to be L-type. Many studies have concluded that Cav1.4, defined by its Cav1.4 pore-forming subunit, is the prominent form in mammalian rods (for review, see Schmitz et al., 2012). This was examined here with two different polyclonal antibodies raised against segments of human (McRory et al., 2004) and mouse Cav1.4 C-termini (see Materials and Methods). Figure 3, *A* and *B*, show that both antibodies give selective and strong labeling of synaptic ribbons in the OPL. The expression of another L-type channel in the synaptic layers was explored with anti-Cav1.3 and an anti-α1Pan (supposedly suited for all Cav1-subunits) was also tested. The anti-α1Pan antibody stained the OPL and showed relatively weaker staining in the IPL (Fig. 3*C*). The anti-Cav1.3 antibody gave intense staining in the IPL, as shown in Figure 3*G*, and no clear staining of photoreceptor ribbons. Closer inspection of the OPL shows that the anti-Cav1.4 antibodies stain the rod ribbons and cones are also marked to a lesser extent (Fig. 3*D*,*E*). The

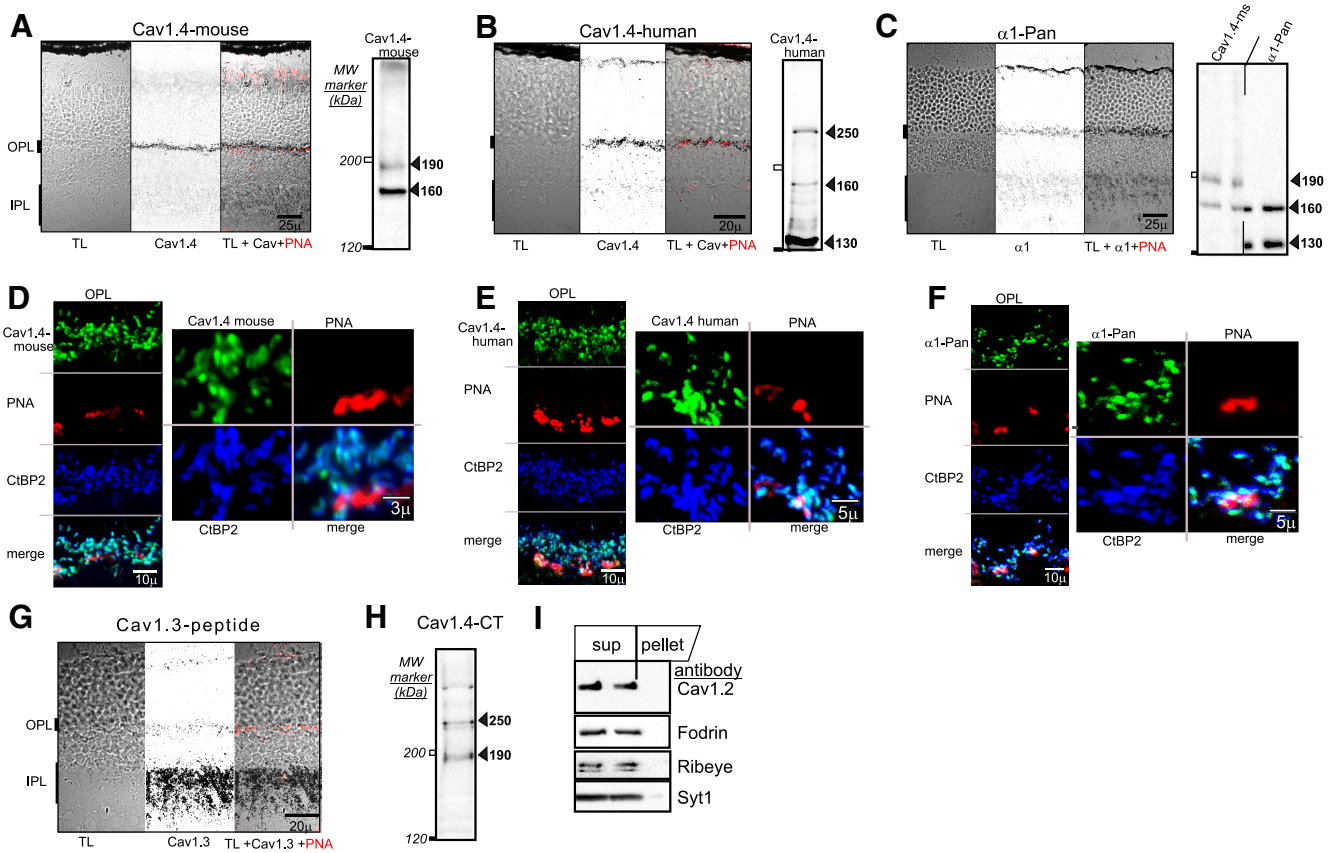

Figure 3. Cav1.4 subunits are preferentially expressed at photoreceptor ribbon synapses. ***A–D***, Cryosections immunostained with different affinity-purified anti-α1 antibodies. The overviews are given as a series of three panels: transmitted light (TL; left) and anti-α1 (excit.: λ488; center), and PNA-Alexa Fluor 568 shown in red. The subsequent color panels display the various probes in the OPL at higher resolution (***D–F***). ***A***, ***B***, Cryosections stained with affinity-purified anti-Cav1.4 mouse and anti-Cav1.4 human antibodies reveals strong labeling in the OPL. ***C***, α1Pan antibody (Alamone Labs) exhibits a slightly stronger preference for OPL over IPL. ***D–F***, Regions of the OPL illustrating the rich association of the Cav1.4-subunit with rod ribbons and perhaps with PNA labels cone terminals. ***G***, Intense staining of the IPL with the α1D-peptide antibody (Alamone Labs) and very little signal specific to the OPL. Mouse retinas were lysed with a detergent-rich buffer to examine Cavα1-subunits with Western analysis. The anti-Cav1.4 mouse antibody yields bands at 160 and 190 kDa (***A***, right side of each lane highlights major bands with filled triangles and, on the left, the migration of the 120 and 200 kDa protein standards are indicated with filled and open rectangles, respectively). In ***B***, the Cav1.4 human antibody gives a prominent band at 250 kDa (McRory et al., 2004) and additional bands at 160 and 130 kDa. ***H***, Anti- Cav1.4-CT peptide detects bands that are similar in size to products detected with the other anti- Cav1.4 antibodies at 190 and 250 kDa. The transfer membrane presented in ***C*** was cut into multiple vertical strips such that split lanes could be exposed to different antibodies and then realigned for comparison during enhanced chemiluminescence exposure. ***C***, Notably, the anti-α1Pan antibody consistently gave bands at 160 and 130 kDa, similar in size to products detected by anti-Cav1.4 human and mouse antibodies. The blot in ***I*** shows that the proteins in the retinal lysate are almost entirely in the supernatant fraction rather than the pellet (samples were loaded in equal proportions).

anti-α1Pan signal is associated with ribbons (Fig. 3*F*), which suggests that it recognizes the Cav1.4-subunit.

Western blots were made from retinal lysates and probed with the different anti-Cav1.4 antibodies to identify the possible forms of Cav1.4. The anti-Cav1.4 human antibody (Fig. 3*B*) and a second Cav1.4-C terminus antibody (referred to as Cav1.4-CT; Fig. 3*H*) consistently recognized a band at 250 kDa similar to the original report of this antibody (McRory et al., 2004). The Cav1.4-CT antibody also generated a band at 190 kDa, which overlaps with a higher-molecular-weight band detected with the anti-Cav1.4-mouse antibody (Fig. 3*A*,*H*). When probing the retinal lysates with the anti-α1-Pan antibody, two bands at 130 and 160 kDa were detected (Fig. 3*I*). Similar 130 and 160 kDa bands were detected by the anti-Cav1.4 human antibody (Fig. 3*B*), and the 160 kDa band was also captured by anti-Cav1.4 mouse antibody (Fig. 3*A*). The anti-Cav1.4 antibodies detect proteins in the range of 130–250 kDa (Fig. 3*A*,*B*,*H*), spanning the range of predicted sizes (Tan et al., 2012), and the bands at 160 and 250 kDa match the sizes reported previously (McRory et al., 2004; Liu et al., 2013) and common to the Cav1.4 antibodies tested here. The Western results suggest that multiple Cav1.4 products exist in the retina, as was proposed previously (Tan et al., 2012), and the immunofluorescence results strongly support the conclusion that the Cav1.4 products are enriched at rod ribbons.

Voltage-dependent calcium currents are nearly eliminated in RIM1/2 cdko mice

Measurements of I_{Ca} were made from rods in retinal slices using a whole-cell voltage-clamp configuration. As noted already, the ONL of the mouse retina is dominated by rods, constituting ~95% of the photoreceptors, and there are 6–12 rows of somata in the ONL. To gain access to the terminal where the Cav1.4 channels are expressed, somata of rods were targeted because they are easier to patch than their small, ~2 μm synaptic terminals. Because slicing can sever the axon bridging the soma to the terminal, two features were used to verify an intact terminal. First, the fluorescent tracer Lucifer Yellow (LY) was added to the intracellular solution to visualize the terminal (Fig. 4*A*,*B*). Second, the occurrence of small synaptic release events indicated a terminal was present (described below). After the experiments, the cells were stained for Cre expression (Fig. 4*A*,*B*).

The rods were probed with voltage ramps at speeds of 0.2 or 1 V/s to attain *I–V* curves and, to avoid activating currents other than I_{Ca}, Ca^{2+}-activated currents were suppressed by adding 10

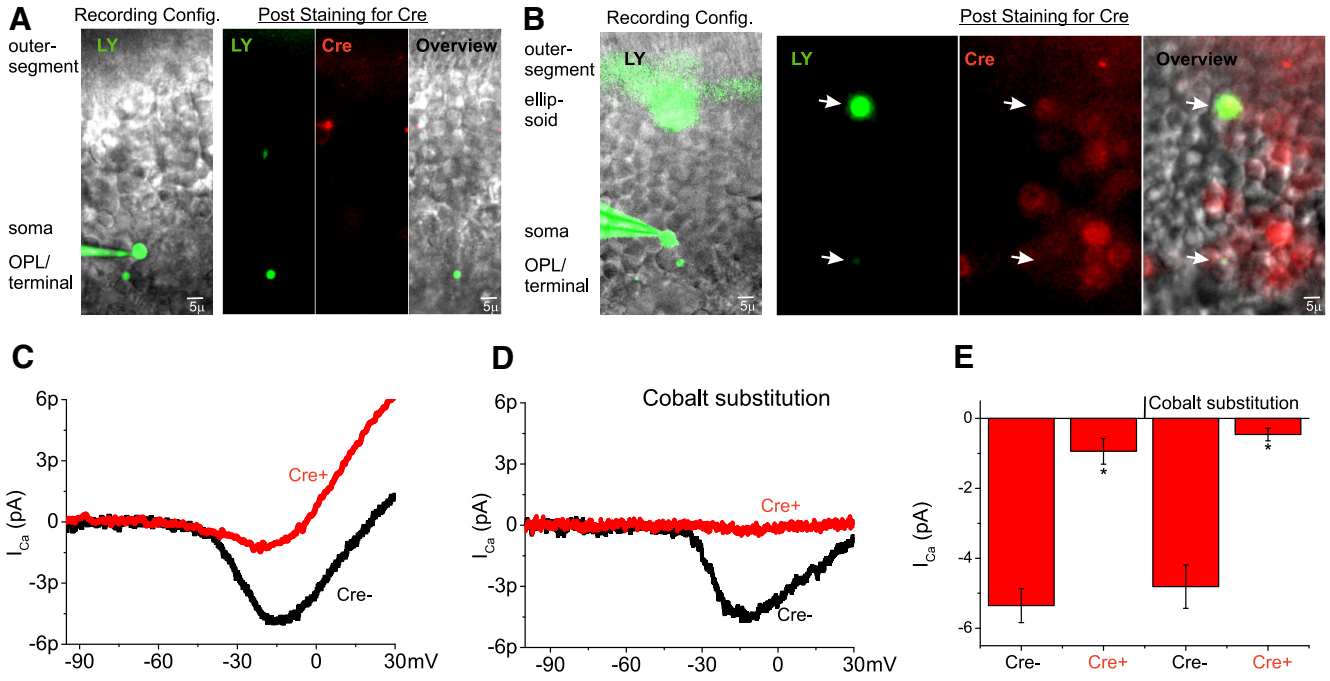

Figure 4. Calcium influx is silenced in the cdko rods. ***A***, ***B***, Series of images illustrating the recording configuration used to make whole-cell voltage-clamp measurements of I_{Ca} from rods and the intracellular labeling and poststaining for Cre. The example in ***A*** shows a control recording made from a Cre rod and the electrode and infused soma–axon terminal are visualized with the cell tracer LY (green), which is overlaid onto the bright-field image (morphological structures are listed on the left side of the panel). The next three panels labeled "post staining for Cre" present the section after staining for Cre. The LY signal reveals the terminal and a small portion of the inner segment and the Cre signal does overlap (red, secondary Ab-Alexa Fluor 568). The combination of the fluorescent signals with the bright-field image is presented in the overview. ***B***, Example of a recording from a cdko rod. Cre $^+$ staining is demonstrated in the cell's ellipsoid (upper arrows) and Cre is also expressed in surrounding areas of the ONL and OPL. Lower arrows track the terminal. ***C***, Average responses to ramps delivered at 1 V/s . ***D***, Average difference currents made from rods recorded in 2 mM $CaCl_2$ and 4 mM $CoCl_2$ and stimulated with a ramp speed of 0.2 V/s. ***E***, graphical summary of results in ***C*** (left) and ***D*** (right, labeled "cobalt substitution").

mM EGTA or 5 mM BAPTA to the intracellular solution. In addition, 5 mM CsCl plus 20 mM TEA were added to the extracellular solution to block I_h and potassium channels, respectively (see Materials and Methods). Recordings from control cells gave similar *I–V* curves when either the fast or slow voltage ramp speeds were used (I_{Ca} for 1 V/s ramps: -5.38 ± 0.48 pA, $V_{m1/2}$: -28 ± 1 mV, $n = 14$; and for 0.2 V/s: maximal I_{Ca} -4.84 ± 0.63 pA; $V_{m1/2}$: -26 ± 3 mV, $n = 10$). In contrast, the maximal I_{Ca} changed drastically in the cdko rods. When the faster ramp speed was used, the average I_{Ca} from cdko responses was -0.94 ± 0.37 pA (6 cells), which is significantly less than what was measured in the control rods ($p < 1E\text{-}6$; tested against 1 V/s controls; Fig. 4*C*). Likewise, the cdko rods tested with the slower ramp speed gave an average maximal I_{Ca} of -0.21 ± 0.05 pA ($n = 8$) that was far less than the control value of -4.84 ± 0.63 pA ($n = 10$) determined with the slower ramp speed ($p < 1E\text{-}5$).

To further characterize the presumed I_{Ca} signal in control and cdko rods, the cells were depolarized at 0.2 V/s in the standard extracellular medium that contained 2 mM $CaCl_2$ and then in a solution containing 4 mM $CoCl_2$ without any added Ca^{2+}. The inward current was eliminated in the recordings made from control mice (all RIM1ff/2ff, $cre^{-/-}$) when Ca^{2+} was removed, but currents measured from cdko cells were not significantly affected by the divalent substitution. This is illustrated by subtracting the ramps taken in $CoCl_2$ from the traces measured in $CaCl_2$ and the resulting difference current reflects the contribution of I_{Ca} to the *I–V* curve. The average difference current derived from control mice had a maximal I_{Ca} of -4.81 ± 0.62 pA and a $V_{m1/2}$ of -26 ± 1 mV ($n = 5$ cells). The difference currents measured from 5 cdko cells averaged -0.46 ± 0.13 pA, which is much smaller than the control group ($p < 0.001$; Fig. 4*D*,*E*). The results from control cells examined with divalent substitution have average I_{Ca} values that are similar to control results that were determined without blocking I_{Ca} and control values are >10-fold higher than the average I_{Ca} determined for cdko rods. Because the cells used to assess I_{Ca} also showed synaptic activity and visible terminals, the lack of an appreciable inward current strongly suggests that very few Cav1.4 channels are operating.

Frequency of miniature glutamate transporter currents is reduced in the RIM1/2 cdko rods

As stated above without proof, synaptic release events measured from rods are associated with the presence of an intact terminal. To demonstrate this, recordings from rods with and without terminals were compared. The image of the cell filled with fluorescent tracer in Figure 5*A* shows the terminal in the OPL and a separate filling of a rod that clearly lacks a terminal is presented in Figure 5*B*. Membrane currents measured at rest (V_{hold}: -80 mV) from the cell with a terminal exhibit spike events that have a rising phase (35–90%: 1.98 ± 0.13 ms; $n = 9$ cells) that is much faster than the decay phase (half-width: 21.6 ± 1.9 ms; $n = 9$ cells; for example events, see Fig. 5*C*,*D*), which fits the general description of a receptor- or transporter-mediated miniature synaptic current. The rod that lacks an attached terminal (Fig. 5*B*) does not exhibit such spikes (Fig. 5*C*), and this holds true in all instances of recordings made from rod somata that were apart from the OPL and dispossessed of their synaptic terminal during slicing ($n = 15$ cells). This demonstrates that the miniature currents are originating from the rod terminal but, to date, there are no published reports of measurements from mouse photoreceptors

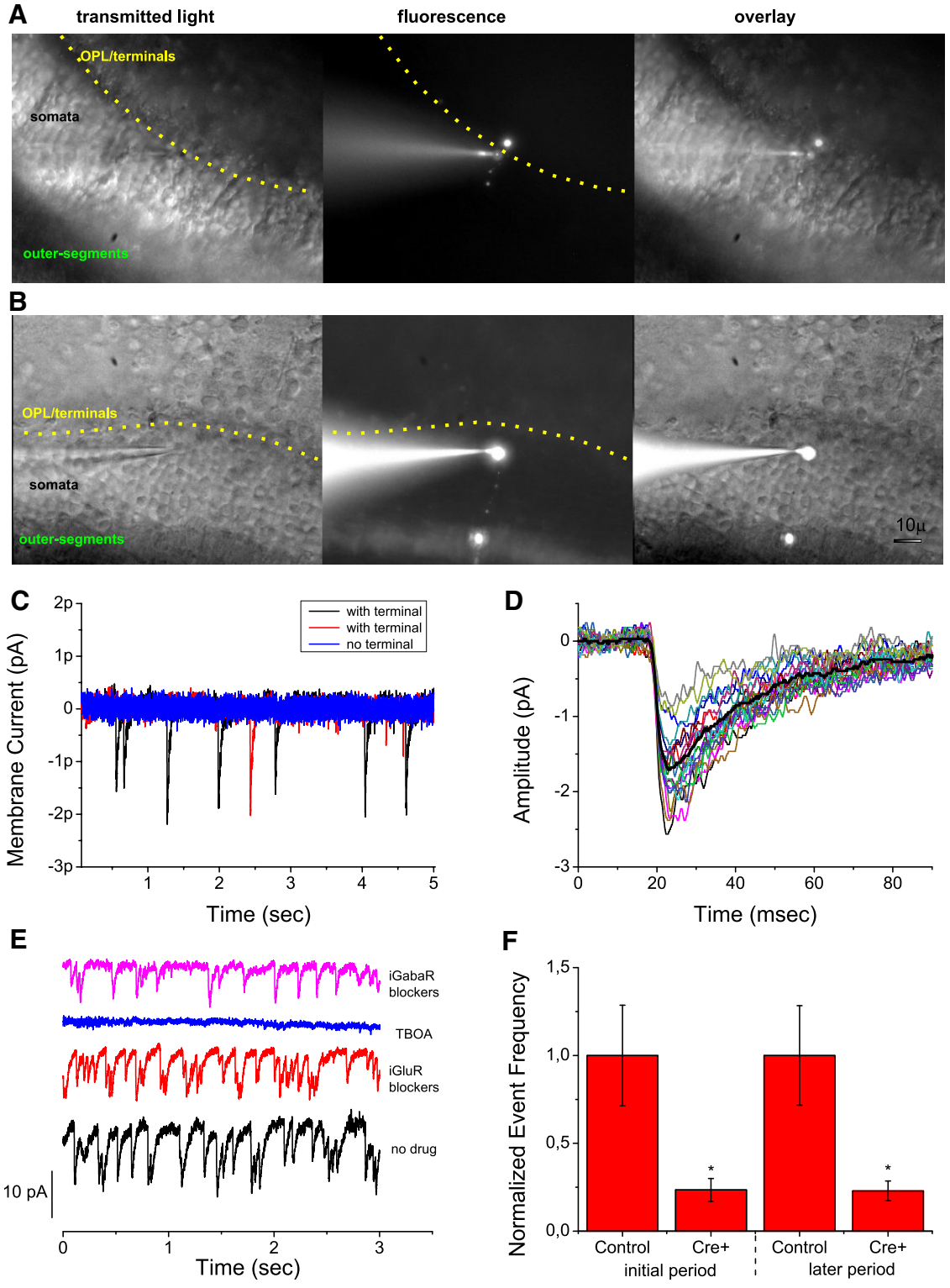

Figure 5. Small synaptic glutamate transporter currents arise from the terminal and are greatly reduced in frequency in the RIM1/2 cdko. ***A***, ***B***, Series of images taken from recordings of rods in the ONL, each starting on the left with transmitted light, and in the center the LY-filled rods; an overlay of the two images is shown on the right. The rod in ***A*** processes a terminal, whereas the example in ***B*** lacks a synaptic ending. ***C***, Membrane current traces with spikes are from the rod with terminal imaged above in ***A***, and the flat trace lacking spikes is from a rod without a terminal featured in ***B***. ***D***, Presents an alignment of miniature events from an individual cell. ***E***, Example of a rod under different pharmacological treatments. The control trace "no drugs" shows miniature synaptic events. The events continue when iGluR inhibitors are added (see Results for specifics on drugs), but in the presence of TBOA, they are silenced. The iGabaR blocker condition followed TBOA and the remergence of events demonstrates the reversibility of TBOA and lack of block by iGABAR blockers. ***F***, Normalized event frequency for control and cdko rods at the indicated sampling periods. During the initial 2 min period, the normalized frequency was 1 ± 0.29 and 0.23 ± 0.07 for control and cdko rods, respectively ($n = 12$ and 9 cells, respectively; $p = 0.016$) and the later period from 3–4 min: 1 ± 0.28 and 0.23 ± 0.06 for control and cdko cells, respectively ($n = 8$ and 7 cells, respectively; $p = 0.012$). Recordings in ***C***, ***D***, and ***F*** were made with 20 mM Cl^- in the intracellular solution, whereas that in ***E*** was performed with potassium thiocyanate in the intracellular solution (see Materials and Methods).

that describe something similar to the small events that we observed.

Previous studies have shown that mouse rods (Hasegawa et al., 2006), ground squirrel cones (Szmajda and Devries, 2011), and turtle (Tachibana and Kaneko, 1988) and salamander (Picaud et al., 1995a; Picaud et al., 1995b) photoreceptors take up glutamate at their terminals where the electrogenic excitatory amino acid transporters (EAATs) are located (Tse et al., 2014). To determine whether EAATs or receptors mediate the miniature events in rods, I_m traces taken shortly after gaining whole-cell access were exposed to a mixture of blockers. The ionotropic glutamate receptor (iGluR) inhibitors (20 μM CNQX for AMPAR/KARs and 50 μM AP-5 to block NMDARs) were applied to five cells and these drugs failed to block the miniature events; likewise, ionotropic GABA receptor blockers (50 μM picrotoxin for GABAR-A, and 20 μM TPMPA for GABAR-C) and glycinergic receptor blocker strychnine (50 μM) were applied to three of the same cells exposed to iGluR inhibitors and these reagents also did not block the miniature events. In contrast, when the EAAT blocker TBOA (200 μM) was applied, the miniature events were entirely silenced ($n = 3$ cells). An example recoding presented in Figure 5*E* illustrates the immunity of the miniature events to all of the receptor inhibitors and the complete block by TBOA. Further support of the miniature events originating from EAATs is the observation that miniature amplitude increased when intracellular chloride (Fig. 5*C*,*D*) was replaced with thiocyanate (Fig. 5*E*), which is the most permeant anion for glutamate transporters (Eliasof and Jahr, 1996).

To determine whether RIM1/2 influenced release frequency, the miniature events were counted in the cdko rods and compared with the control condition. During the initial 2.5 min after cell rupture, the average event frequency was 2.85 ± 0.71 and 0.65 ± 0.16 Hz for the control ($n = 12$) and cdko ($n = 9$), respectively, which was significantly different ($p = 0.016$). Event frequency continued to decline in both the cdko and wild-type conditions, presumably as the terminal filled with Ca^{2+} chelator, and the frequency over the period between 3 and 4 min after entry was again significantly different for the control and cdko rods, with 0.64 ± 0.18 and 0.15 ± 0.04 Hz for the control ($n = 8$) and cdko ($n = 7$) conditions, respectively ($p = 0.013$). In both time frames, the controls maintained a 4-fold greater rate of release relative to the cdko rods (Fig. 5*F*). Presumably a reduction in Cav1.4 channel openings in the cdko rods reduced the amount of free intracellular Ca^{2+} needed for release, leading to a lower frequency of miniature transporter currents.

Membrane capacitance measurements from RIM1/2 cdko rods reveal a loss of voltage-dependent release

The results show that RIMs are needed to maintain normal I_{Ca} influx and the outcome for the cdko is predicted to lead to a decrease in Cav1.4 channel-mediated Ca^{2+}-dependent release. To investigate this possibility directly, stimulated vesicular fusion was monitored by measuring the synaptic terminal's C_m in response to step depolarizations. The somata of rods located directly next to the OPL were targeted (Fig. 6*A*,*B*) because they contain the ribbon within their soma compartment (see Materials and Methods). Recordings from control and cdko rod somata exhibit miniature events (Fig. 6*C*), as described earlier (Fig. 4*C*), and voltage ramps produced I_{Ca} *I–V* profiles (Fig. 6*D*) similar to the situation described for recordings of I_{Ca} in more intact cells (Fig. 4*F*). When the cells were depolarized for 0.2 s, the controls responded with significantly more release, with controls showing a 1.7 ± 0.3 fF jump in C_m and the cdko rods 0.1 ± 0.02 fF ($p < 0.0001$; Fig. 2*C*,*D*). Average changes in C_m for 1 s steps stimulated 2.9 ± 0.5 fF and 0.4 ± 0.1 fF of vesicle fusion from control and cdko cells, respectively ($p < 0.0001$; 6 control and 8 cdko; Fig. 6*G*,*H*). The results illustrate that voltage-dependent evoked release is greatly impaired in the absence of RIM1/2.

Estimating the potential number of docked vesicles at the ribbon base

EM images of rod terminals were analyzed to determine the density and size of synaptic vesicles (SVs) along its ribbon (Fig. 6*I*) and the values were used to estimate the number of fusing vesicles (see Discussion). Vesicle diameters fell within a narrow range of sizes (23–40 nm) and had an average diameter of 32.5 ± 0.6 nm (7 cells, 5–10 profiles measured from each ribbon). The vesicles are tightly packed along the ribbon, as illustrated in Figure 6*J*, where the SVs appear to be touching one another or even overlapping within an ultrathin section of ~60 nm. Assuming that the vesicles are packed at maximal density (see Materials and Methods), we estimate that 43 vesicles pack per row on each face of the ribbon, with a total of 10 rows on a ribbon, amounting to 860 vesicles/ribbon (see Materials and Methods). To derive the number of fusing vesicles per ribbon, we divided the evoked change in C_m by the single vesicle capacitance of 35 aF that was calculated from vesicle diameter (32 nm) and published measurements of single vesicle capacitance (Neef et al., 2007, and see our Materials and Methods). The control cell responses of 1.7 and 2.9 fF elicited with 0.2 and 1 s stimulations equal 49 and 83 vesicles, respectively.

Cav1.4 channels are normally expressed at ribbons in RIM1/2 cdko rods

Either a lower probability of channel openings or degradation of the channels may underlie the lack of I_{Ca} observed in the RIM1/2 cdko. To determine whether channel expression was reduced, retinal sections were costained for the pore-forming Cav1.4 subunit of Cav1.4 and the ribbon protein Ribeye (Schmitz et al., 2000) relative to Cre and PNA. Regions rich in Cre showed strong labeling of Cav1.4 across the OPL comparable to regions without Cre when the anti-Cav1.4 human antibody was used (Fig. 7*A–E*), and inclusion of PNA to mark cones shows that the Cav1.4 staining localized to rod ribbons was dense (Fig. 7*F*,*G*). The α1-Pan antibody gave similar results (Fig. 7*H*). The results show no regional loss of Cav1.4 at ribbons in Cre-poor and Cre-rich regions of the photoreceptor layer and, at higher resolution, Cav1.4 labeling maintains a U-shaped profile around the ribbon protein Ribeye. The staining for Ribeye also appears normal when RIM2 is absent (Fig. 7*I*,*J*).

Western blot results show that the level of Cav1.4 detected in retinal extracts was normal in cdko retinas at 4–8 weeks and in much older mice at 3 and 9 months (Fig. 7*K–M*). The densitometry measurements of the 160 kDa Cav1.4 band generated from control and cdko retinas were not significantly different (control vs cdko, normalized mean ± SE: 0.94 ± 0.08 vs 1.0 ± 0.07) and the 250 kDa band was also unchanged in the cdko samples (control vs cdko: 1.0 ± 0.06 vs 0.97 ± 0.05; Fig. 7*K–M*). Very similar results were obtained when using retinas from older mice (160 kDa band, control vs cdko: 1.0 ± 0.06 vs 0.94 ± 0.12; and the 250 kDa band, 0.96 ± 0.06 vs 1.0 ± 0.04; 3 litters were used for each age group; Fig. 7*M*). Because Cav1.4 is expressed exclusively in the OPL (Fig. 3*A*,*B*), the Western analysis reflects the situation for Cav1.4 in the OPL.

No changes in Cav1.4 expression levels were observed in retinas from cdko mice, nor is there evidence for a redistribution of

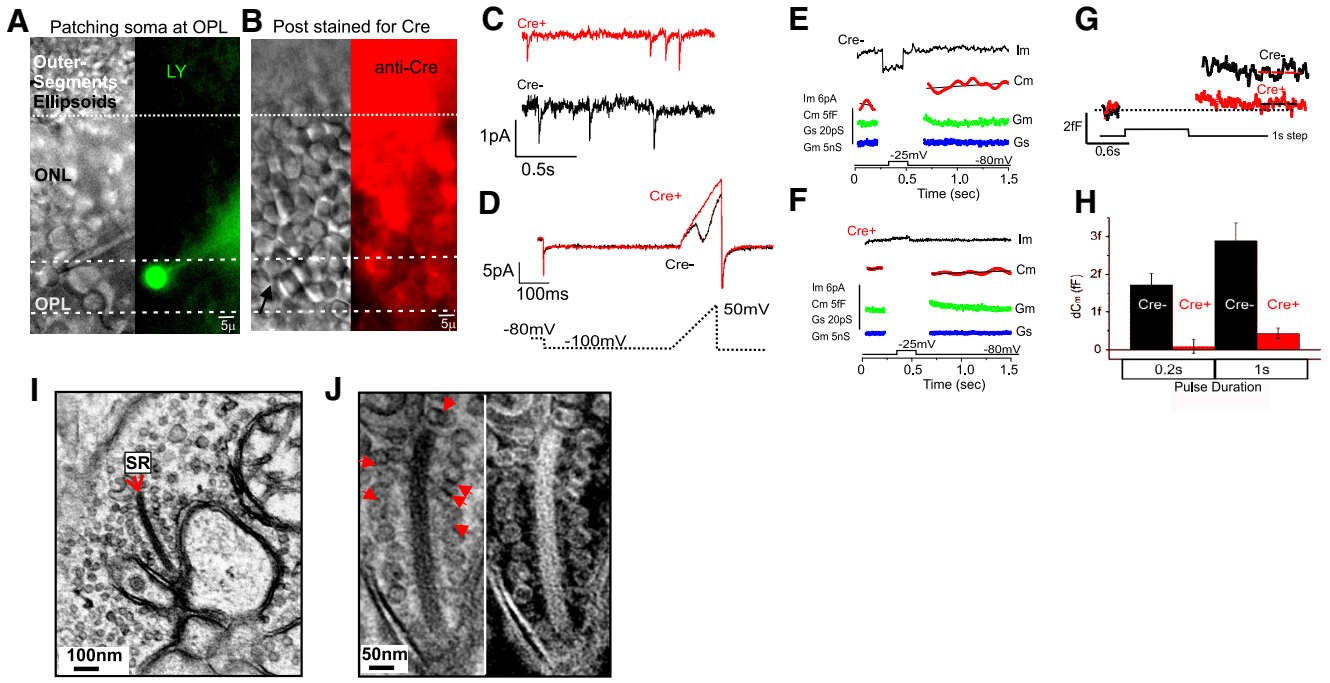

Figure 6. Loss of RIM1/2 nearly abolishes stimulated release from rods. ***A***, Shows a bright-field image of a patch-clamp electrode contacting a rod soma at the OPL and the fluorescent image is overlaid to show the electrode soma filled with LY (green). ***B***, The same region was reimaged after the section was immunolabeled with anti-Cre (Cre in red), and the arrow indicates the cell's soma location in a region that stains heavily for Cre. In ***C–F*** are pairs of recordings from the RIM1/2 cdko in ***A*** and a control cell (RIM1ff/2ff, LMOP*cre*$^{-/-}$). ***C***, Whole-cell membrane current traces with spontaneous release events from the control and cdko cells. ***D***, Voltage sweeps showing an absence of inward calcium current in the cdko and ~−5 pA inward current for the control, whereas other aspects of the current traces are similar (ramp protocol: start at −80 mV, stepped to down −100 mV for 0.5 s, and the ramp rose to +50 mV at 1 V/s). ***E***, ***F***, Evoked release was assessed with steps from rest (−80 mV) to a depolarizing voltage of −25 mV for 200 ms, which produced an ~1.5 fF jump in C_m for the control (***E***) and no obvious change in C_m for the cdko (***F***, black lines represent linear fits to C_m traces prestimulation and poststimulation to illustrate the average). The control has an I_m during the step that reflects Ca^{2+} entry, whereas the cdko cell lacked an inward current. G_s was unaltered and G_m was momentarily elevated after the depolarization and settled by 0.75 s poststimulus (C_m was averaged from 0.75–1 s poststimulus). ***G***, Control and cdko average C_m traces for 0.2 and 1 s depolarizations (dotted lines spanning C_m traces indicate the baseline). ***H***, C_m measurements for control and cdko cells given 0.2 and 1 s steps. ***I***, EM image of a rod terminal that captures its singular synaptic ribbon (designated SR) with its rich cache of synaptic vesicles (wild-type mouse) and in the top left corner the nuclear envelop appears. ***J***, Pair of images of the same ribbon in ***I*** at higher magnification, with the transmitted, conventional image on the left, and its inverted version is shown on the right to give an alternative impression. The images emphasize the dense, elbow-to-elbow packing of synaptic vesicles along the ribbon and overlapping vesicle profiles (indicated with red arrows). The electrophysiological recordings to stimulate dC_m were performed with 2 mM EGTA in the pipette and traces were low-pass filtered at the following corner frequencies for presentation and analyses: I_m: 200 Hz, C_m: 10 Hz, G_m: 100 Hz, and G_s: 100 Hz.

protein away from the terminals; however, it is possible that ribbon size was altered. To examine this possibility, ribbon contour lengths were measured in sections made from control and cdko retinas and the sections were costained with multiple antibodies, as described already. Ribbon contour lengths were unchanged in the Cre-rich regions of cdko retinas regardless of the antigen tested: Ribeye (control vs cdko), 1.62 ± 0.05 vs 1.61 ± 0.07 μm; Cav1.4, 1.46 ± 0.06 vs 1.58 ± 0.08 μm ($p = 0.21$); and RIM2 present in controls, 1.45 ± 0.09 μm (3–4 animals per condition at ages of +8 wks; Fig. 7*N*). In total, we demonstrate that Cav1.4 is normally expressed in cdko retinas and the ribbon synapse, as judged by Ribeye staining, is also unchanged.

RIM2 does not alter the expression of Cav1.4 currents when assessed in HEK cells

The expression levels of Cav1.4 and its targeting to the synapse were not altered in the absence of RIM1/2. Previous studies have suggested that long forms of RIM1/2 can influence the expression levels of Cav1.4 as determined by membrane current density (Miki et al., 2007). To explore this possibility, we overexpressed RIM2α with Cav1.4 (Cav1.4, Cavβ_{2a}, and Cav$\alpha_2\delta$-1) in HEK cells and performed standard electrophysiological measurements of whole-cell currents in 20 mM $BaCl_2$ to ensure that Ca^{2+}-dependent processes were not invoked. The control condition with Cav1.4 alone gave a similar maximal conductance to the situation with Cav1.4 + RIM2 (control vs +RIM2: 0.41 ± 0.06 vs 0.39 ± 0.06 nS), and the $V_{1/2}$ was not significantly different ($V_{1/2}$ for control vs +RIM2: 6.04 ± 1.77 vs 9.26 ± 2.35 mV; $p = 0.17$; $n = 15$ and 10 cells; Fig. 8). The results demonstrate that the current density is not altered by the presence RIM2 in this controlled condition.

Discussion

For rod photoreceptors to communicate with postsynaptic bipolar and horizontal cells in a regulated manner, glutamate-filled vesicles in the rod's terminal must fuse with the plasma membrane and release transmitter onto the postsynaptic targets at the appropriate time. The primary trigger for exocytosis is Ca^{2+}, so the regulated opening of Cav1.4 at the ribbon active zone will have a central role in scheduling Ca^{2+}-dependent glutamate release. Investigators have identified >50 mutations affecting the Cav1.4 subunit that are associated with incomplete CSNB in humans and other animals (Lodha et al., 2012). *In vitro* studies often reveal that these mutant forms of Cav1.4 exhibit reduced Ca^{2+} currents or the channels open at a more positive voltage, which leads to less Ca^{2+} entry over physiological voltages (McRory et al., 2004; Hemara-Wahanui et al., 2005; Hoda et al., 2005). ERGs from animals carrying certain mutations in, or completely lacking, the Cav1.4 subunit show a reduction in synaptic transmission between rods and rod bipolar cells under low light levels

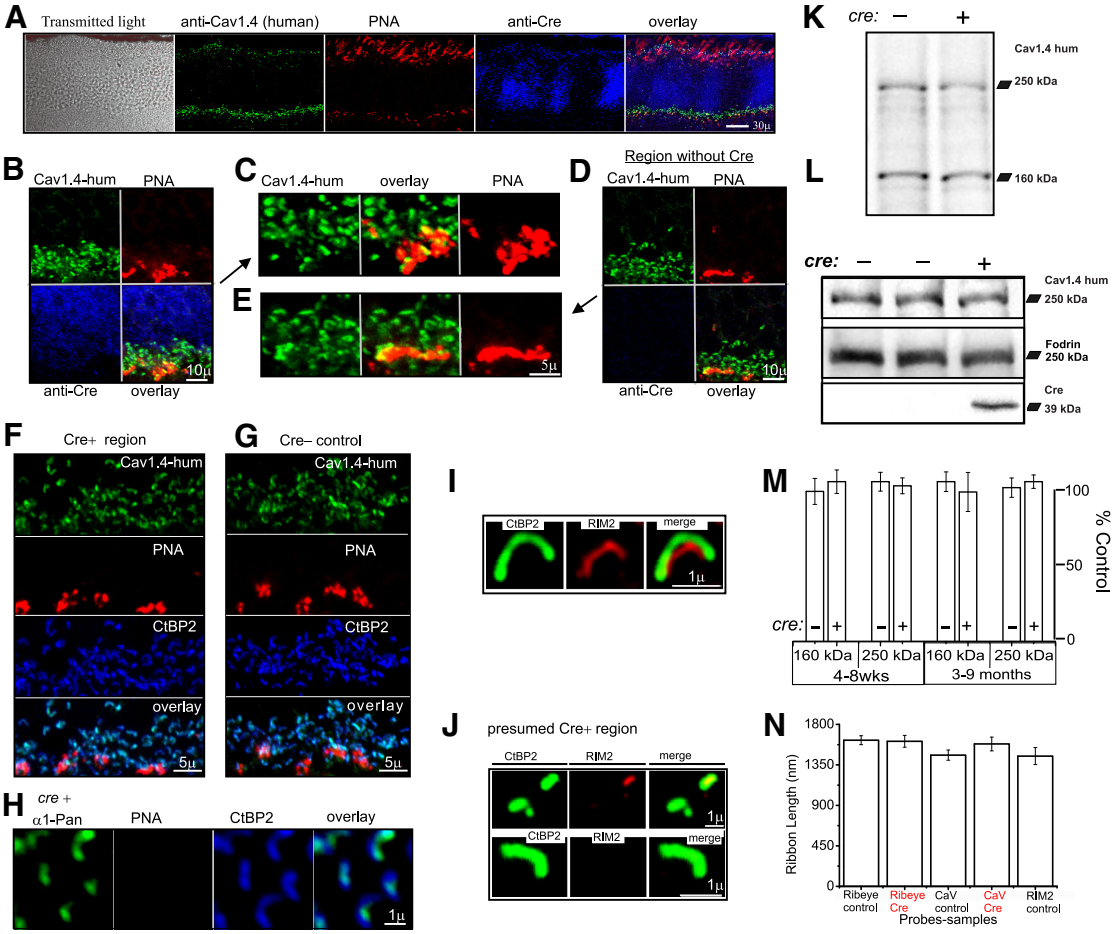

Figure 7. Expression of Cav1.4 remains normal in the absence of RIM2. ***A***, Overview of colabeling for Cre, Cav1.4 subunit and PNA at 9 weeks. ***B***, Area of the ONL that is heavily stained for Cre and a dense layer of Cav1.4 signal is shown to persist. ***C***, Subregion from ***B*** presented at higher resolution shows the ribbon-like shape of the Cav1.4 signal. ***D***, Area without Cre taken from a region neighboring ***B***. ***E***, Portion of the image from ***D*** examined at higher resolution. ***F–H***, Costaining with the addition of CtBP2 to independently mark Ribeye/ribbons (mice were 9 weeks of age). ***F***, ***G***, Sections from RIM1/2 cdko and control littermates showing strong labeling at ribbons regardless of Cre expression. ***I***, Semithin section (see Materials and Methods) from a *cre* $^{+}$ animal that shows normal staining of RIM2 in a presumably Cre poor region. ***J***, Area reduced in RIM2 that is presumed to be a Cre $^{+}$ region (only a small portion shows RIM2 signal in the top, possibly a cone ribbon). Notably, in ***J***, the anti-CtBP2 staining of Ribeye gives normal ribbons even in the absence of RIM2. ***K***, ***L***, Western blots comparing littermates that are 4 weeks (***K***) and 3 months (***L***) of age, which do not indicate a gross loss of Cav1.4 subunit expression. ***M***, Summary of Western densitometry results obtained with Cav1.4 human (250 and 160 kDa bands) and Cav1.4 mouse (160 kDa band) antibodies using mice at the ages indicated in the graph (see Fig. 2 for a summary of synaptic probes at 3 months). ***N***, Ribbon length was measured from cryostat retinal sections stained for Ribeye (anti-CtBP2), anti-Cav (anti-Cav1.4-human or α1PAN), and anti-RIM2. Samples were from control (*cre* $^{-/-}$) animals or Cre $^{+}$ expressing regions of cdko samples.

when rods are needed for vision (Doering et al., 2008; Liu et al., 2013; Michalakis et al., 2014). These examples involve mutations in Cav1.4, but in many instances, the functional deficit results from the channel failing to effectively interact with other proteins such as adaptor/modulator proteins (for review see, Simms and Zamponi, 2014).

Our study is the first demonstration of Cav1.4 channels in a neuronal preparation being dependent on RIM1/2 for normal operation. By making electrophysiological recordings from rod synaptic terminals, we were able to monitor I_{Ca} directly under voltage-clamp conditions and show that I_{Ca} is nearly eliminated in RIM1/2 cdko mice (Fig. 4*D*). The bulk of the research on RIM1/2 has documented changes in postsynaptic responses after the removal of RIM1/2 from presynapses enriched in P/Q and *N*-type Cav channels (for review, see Südhof, 2012), but only two other groups of investigators have made recordings directly from the presynaptic terminals using a whole-cell voltage clamp configuration (Han et al., 2011; Han et al., 2015; Jung et al., 2015). Importantly, Han et al. (2011) reported a ~2- to 3-fold reduction in P/Q and *N*-type I_{Ca} at the calyx of Held in the RIM1/2 cdko, comparable to what has been witnessed for Cav1.3-expressing cochlear hair cells with RIM1/2 deleted (Jung et al., 2015). Separate studies examining the role of RIM have used fast Ca^{2+} imaging methods to monitor the change in presynaptic Ca^{2+} fluorescence in response to action potentials and also found that deletion of RIM caused a reduction in peak Ca^{2+} fluorescence, dropping by ~40% (Kaeser et al., 2011; Müller et al., 2012) or 25% (Kintscher et al., 2013). Our study is consistent with these reports in having witnessed a reduction in I_{Ca} when RIM1/2 were deleted and, when I_{Ca} was assessed with voltage-clamp conditions, the affect is greatest and more consistent with our observation.

Because removal of RIM from rods abrogated voltage-dependent Ca^{2+} entry, we examined the expression levels of Cav1.4 in the RIM1/2 cdko mice to determine whether the channels were removed from the synapse or if they were degraded. Western analysis of Cav1.4 protein levels in control and cdko retinas did not reveal a difference between the two groups (Fig. 7*M*) and the dimensions of the synaptic ribbon when stained for with Ribeye and Cav1.4 antibodies were unaltered in the cdko

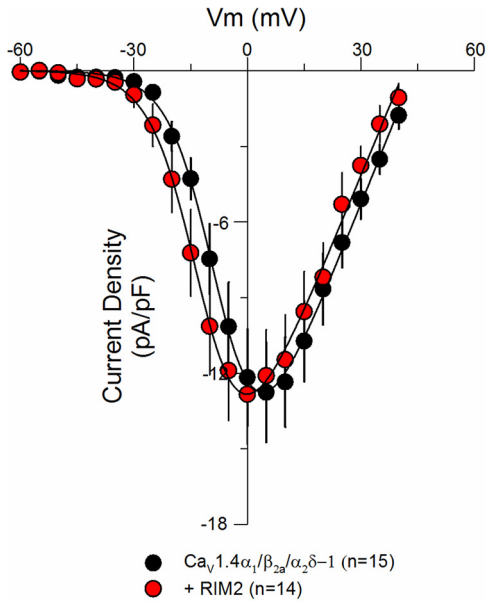

Figure 8. Overexpression of RIM2α does not alter the expression of Cav1.4 in cultured tsA-201 cells. Average *I–V* plots for the control condition that consisted of the indicated Cav1.4 subunits are compared to the results attained from the coexpression of Cav1.4+RIM2α.

mice (Fig. 7*N*); notably, we used three different Cav1.4 antibodies to examine Cav1.4 (Figs. 3, 7) and the Cav1.4 profiles in cdko rods appear ribbon shaped. These findings support the conclusion that the opening of Cav1.4 is facilitated by RIM1/2, but maintenance of the channel at the ribbon, and the ribbon itself are not dependent on RIM1/2 (Fig. 7*N*). An earlier report that focused on the influence of RIM1α on Cav1.4 found an increase in current density when the two were coexpressed in HEK cells (Kiyonaka et al., 2007); however, our heterologous coexpression of RIM2α with Cav1.4 failed to show a role for RIM2α in altering surface expression of the channel as estimated from Cav1.4 current density (Fig. 8), which again suggests that RIM2α is not essential for Cav1.4 trafficking. It is possible that the positive regulation of Cav1.4 by RIM2α at the synapse is dependent on an additional active zone protein(s) and the role of RIM2 may be to bring the channel into an interaction with a positive modulator or promote posttranslational modifications of the channels that enhances their opening. Alternatively, RIM2 may prevent inhibition of CaV1.4 by blocking mechanisms that downregulate channel function. In either instance, RIM2 would be serving as a scaffolding protein that modulates Cav1.4 function, albeit indirectly, and without any role in channel trafficking to the synapse. Further work will be required to elucidate the molecular basis of the positive modulator effect of RIM2 on Cav1.4 and whether it is a direct interaction or mediated in part by other factors. An obvious starting point would be to explore the several possible combinations of Cav1.4 subunits involving variants of the α- and β-subunits that are unique to photoreceptors (Tan et al., 2012; Lee et al., 2015) and assess whether they create a more direct modulator role for RIM2.

Previous studies did not report a shift in active zone markers when RIM was removed (Kaeser et al., 2011; Graf et al., 2012; Jung et al., 2015), but a portion of Cav2.1 and 2.2 channels were mislocalized when RIM1/2 were deleted (Kaeser et al., 2011), Cav1.3 clustering was reduced when RIM2α was removed from inner hair cells (Jung et al., 2015), and clustering of Cav channels at the *Drosophila* NMJ was reduced in the knock-out (Graf et al., 2012). Whether channels were mislocalized without a change in the overall level of Cav channel expression was not determined, but assuming that channel numbers remained the same because mRNA levels were reported to be unaltered in RIM1/2 cdkos (Kaeser et al., 2011), then the absence of an interaction with RIM1/2 may have created channels that were no longer permitting Ca^{2+} entry, which would agree with our interpretation that RIM facilitates channel opening at the active zone. The compound effect of channel mislocalization and reduced Ca^{2+} accumulation has a significant or even profound impact on responses measured from the postsynapse (Castillo et al., 2002; Schoch et al., 2002; Kaeser et al., 2011; Graf et al., 2012; Müller et al., 2012; Han et al., 2015) and presynapse (Jung et al., 2015). In an effort to pin the changes squarely on the presynapse, we chose to measure depolarization-evoked changes in the rod membrane capacitance, which offers a better readout of the number of fusing vesicles.

The mouse rod is unique in that it expresses a single ribbon, whereas cones in the mouse retina and photoreceptors in other animals fill their terminals with multiple ribbons (Thoreson et al., 2004; Li and DeVries, 2006). The small size of the rod presents a technical challenge, but the benefit is that any change in release, and likewise I_{Ca}, can be attributed to the activity at a single synaptic ribbon. We report that the control rods release 49 and 83 vesicles when elicited with 0.2 and 1 s stimulations, respectively (Fig. 6*H*). The control results suggest that a rod ribbon releases with an efficiency similar to ribbons in other retinal preparations. For comparison, a salamander cone may release 50–100 vesicles/s per ribbon and the mouse On-rod bipolar cell can discharge ~30–60 vesicles/s per ribbon, which is driven by an average I_{Ca} value <1 pA/ribbon (for review, see Wan and Heidelberger, 2011).

Relating the physiological data to synaptic ribbon structure creates a spatial context for the releasable pool of vesicles. If we assume the vesicles are packed along the ribbon at maximal density (Fig. 6*I*,*J*), then 86 vesicles will occupy each row starting at the ribbon arciform density, totaling 860 vesicles per ribbon (see Materials and Methods), which is a higher number than the 55–65 vesicles at the arciform and ~350 per ribbon that was previously measured (Zampighi et al., 2011). Our results suggest that a 0.2 s stimulation may be sufficient to release a significant portion of the first row of vesicles. The number of Cav1.4 channels involved can be predicted from published work that measured I_{Ca} from cultured cells expressing Cav1.4, which revealed the channels have a very low open probability (<~0.002 at −20 mV) and an exceptionally small single-channel conductance (between 1 and 4 pS), which would pass 0.03–0.1 pA per channel at −25 mV (Doering et al., 2005). Our results in Figure 8 show a lack of change in maximal conductance when RIM2α is coexpressed with Cav1.4, which is likely to extend to single-channel behavior. Therefore, the 5 pA I_{Ca} measured at a ribbon could reflect 50–200 channels opened at a given time. If we assume that 200 Cav1.4 channels open near the 49 fusing vesicles at the base of the ribbon, then ~4 Cav1.4 channels drive the release of a vesicle (a similar situation has been described for inner hair cell ribbon synapses, where 4–8 Cav channels are proposed to support release of a vesicle; Zampini et al., 2010). The RIM1/2 cdko rods, which gave ~0.4 pA of current (Fig. 4*E*), may represent 16 Cav channels participating in the release of ~3 vesicles (0.1 fF) after a 0.2 s depolarization; therefore, ~5 Cav channels are needed to release a vesicle from the cdko rod, which is similar to the ratio in wild-type rods.

We show here that long forms of RIM1/2 are essential for the influx of Ca^{2+} into mouse rod terminals, which endows RIM1/2

with the capacity to facilitate release. We demonstrate this by assaying I_{Ca} and monitoring membrane capacitance and miniature transporter events directly from individual rod ribbons that possess or lack RIM1/2. In general, a facilitative role for RIM1/2 appears to hold across many synapses (Südhof, 2012). However, our results point to a unique role for RIM1/2 in facilitating Cav1.4 openings in a way that expands the functional size of the ribbon active zone—and this occurs without changing the localization of Cav1.4 around the ribbon.

References

Bader CR, Bertrand D, Schwartz EA (1982) Voltage-activated and calcium-activated currents studied in solitary rod inner segments from the salamander retina. J Physiol 331:253–284. CrossRef Medline

Boycott KM, Maybaum TA, Naylor MJ, Weleber RG, Robitaille J, Miyake Y, Bergen AA, Pierpont ME, Pearce WG, Bech-Hansen NT (2001) A summary of 20 CACNA1F mutations identified in 36 families with incomplete X-linked congenital stationary night blindness, and characterization of splice variants. Hum Genet 108:91–97. CrossRef Medline

Castillo PE, Schoch S, Schmitz F, Südhof TC, Malenka RC (2002) RIM1alpha is required for presynaptic long-term potentiation. Nature 415:327–330. CrossRef Medline

Dembla M, Wahl S, Katiyar R, Schmitz F (2014) ArfGAP3 is a component of the photoreceptor synaptic ribbon complex and forms an NAD(H)-regulated, redox-sensitive complex with RIBEYE that is important for endocytosis. J Neurosci 34:5245–5260. CrossRef Medline

DeVries SH (2001) Exocytosed protons feedback to suppress the Ca2+ current in mammalian cone photoreceptors. Neuron 32:1107–1117. CrossRef Medline

Doering CJ, Hamid J, Simms B, McRory JE, Zamponi GW (2005) Cav1.4 encodes a calcium channel with low open probability and unitary conductance. Biophys J 89:3042–3048. CrossRef Medline

Doering CJ, Rehak R, Bonfield S, Peloquin JB, Stell WK, Mema SC, Sauvé Y, McRory JE (2008) Modified Ca(v)1.4 expression in the Cacna1f(nob2) mouse due to alternative splicing of an ETn inserted in exon 2. PLoS One 3:e2538. CrossRef Medline

Eliasof S, Jahr CE (1996) Retinal glial cell glutamate transporter is coupled to an anionic conductance. Proc Natl Acad Sci U S A 93:4153–4158. CrossRef Medline

Grabner CP, Zenisek D (2013) Amperometric resolution of a prespike stammer and evoked phases of fast release from retinal bipolar cells. J Neurosci 33:8144–8158. CrossRef Medline

Grabner CP, Price SD, Lysakowski A, Fox AP (2005) Mouse chromaffin cells have two populations of dense core vesicles. J Neurophysiol 94:2093–2104. CrossRef Medline

Graf ER, Valakh V, Wright CM, Wu C, Liu Z, Zhang YQ, DiAntonio A (2012) RIM promotes calcium channel accumulation at active zones of the *Drosophila* neuromuscular junction. J Neurosci 32:16586–16596. CrossRef Medline

Grimm C, Wenzel A, Hafezi F, Yu S, Redmond TM, Remé CE (2000) Protection of Rpe65-deficient mice identifies rhodopsin as a mediator of light-induced retinal degeneration. Nat Genet 25:63–66. CrossRef Medline

Han Y, Kaeser PS, Südhof TC, Schneggenburger R (2011) RIM determines Ca(2)+ channel density and vesicle docking at the presynaptic active zone. Neuron 69:304–316. CrossRef Medline

Han Y, Babai N, Kaeser P, Südhof TC, Schneggenburger R (2015) RIM1 and RIM2 redundantly determine Ca2+ channel density and readily releasable pool size at a large hindbrain synapse. J Neurophysiol 113:255–263. CrossRef Medline

Hasegawa J, Obara T, Tanaka K, Tachibana M (2006) High-density presynaptic transporters are required for glutamate removal from the first visual synapse. Neuron 50:63–74. CrossRef Medline

Hemara-Wahanui A, Berjukow S, Hope CI, Dearden PK, Wu SB, Wilson-Wheeler J, Sharp DM, Lundon-Treweek P, Clover GM, Hoda JC, Striessnig J, Marksteiner R, Hering S, Maw MA (2005) A CACNA1F mutation identified in an X-linked retinal disorder shifts the voltage dependence of Cav1.4 channel activation. Proc Natl Acad Sci U S A 102:7553–7558. CrossRef Medline

Hoda JC, Zaghetto F, Koschak A, Striessnig J (2005) Congenital stationary night blindness type 2 mutations S229P, G369D, L1068P, and W1440X alter channel gating or functional expression of Ca(v)1.4 L-type Ca2+ channels. J Neurosci 25:252–259. CrossRef Medline

Jung S, Oshima-Takago T, Chakrabarti R, Wong AB, Jing Z, Yamanbaeva G, Picher MM, Wojcik SM, Göttfert F, Predoehl F, Michel K, Hell SW, Schoch S, Strenzke N, Wichmann C, Moser T (2015) Rab3-interacting molecules 2alpha and 2beta promote the abundance of voltage-gated CaV1.3 Ca2+ channels at hair cell active zones. Proc Natl Acad Sci U S A 112:E3141–E3149. CrossRef Medline

Kaeser PS, Kwon HB, Chiu CQ, Deng L, Castillo PE, Südhof TC (2008) RIM1alpha and RIM1beta are synthesized from distinct promoters of the RIM1 gene to mediate differential but overlapping synaptic functions. J Neurosci 28:13435–13447. CrossRef Medline

Kaeser PS, Deng L, Wang Y, Dulubova I, Liu X, Rizo J, Südhof TC (2011) RIM proteins tether Ca2+ channels to presynaptic active zones via a direct PDZ-domain interaction. Cell 144:282–295. CrossRef Medline

Kintscher M, Wozny C, Johenning FW, Schmitz D, Breustedt J (2013) Role of RIM1alpha in short- and long-term synaptic plasticity at cerebellar parallel fibres. Nat Commun 4:2392. Medline

Kiser PD, Golczak M, Maeda A, Palczewski K (2012) Key enzymes of the retinoid (visual) cycle in vertebrate retina. Biochim Biophys Acta 1821:137–151. CrossRef Medline

Kiyonaka S, Wakamori M, Miki T, Uriu Y, Nonaka M, Bito H, Beedle AM, Mori E, Hara Y, De Waard M, Kanagawa M, Itakura M, Takahashi M, Campbell KP, Mori Y (2007) RIM1 confers sustained activity and neurotransmitter vesicle anchoring to presynaptic Ca2+ channels. Nat Neurosci 10:691–701. CrossRef Medline

Le YZ, Zheng L, Zheng W, Ash JD, Agbaga MP, Zhu M, Anderson RE (2006) Mouse opsin promoter-directed Cre recombinase expression in transgenic mice. Mol Vis 12:389–398. Medline

Lee A, Wang S, Williams B, Hagen J, Scheetz TE, Haeseleer F (2015) Characterization of Cav1.4 Complexes (alpha11.4, beta2, alpha2delta4) in HEK293T cells and in the Retina. J Biol Chem 290:1505–1521. Medline

Li W, DeVries SH (2006) Bipolar cell pathways for color and luminance vision in a dichromatic mammalian retina. Nat Neurosci 9:669–675. CrossRef Medline

Limbach C, Laue MM, Wang X, Hu B, Thiede N, Hultqvist G, Kilimann MW (2011) Molecular in situ topology of Aczonin/Piccolo and associated proteins at the mammalian neurotransmitter release site. Proc Natl Acad Sci U S A 108:E392–E401. CrossRef Medline

Liu X, Kerov V, Haeseleer F, Majumder A, Artemyev N, Baker SA, Lee A (2013) Dysregulation of Ca 1.4 channels disrupts the maturation of photoreceptor synaptic ribbons in congenital stationary night blindness type 2. Channels (Austin) 7:514–523. CrossRef Medline

Lodha N, Loucks CM, Beaulieu C, Parboosingh JS, Bech-Hansen NT (2012) Congenital stationary night blindness: mutation update and clinical variability. Adv Exp Med Biol 723:371–379. CrossRef Medline

Makino CL, Wen XH, Michaud N, Peshenko IV, Pawlyk B, Brush RS, Soloviev M, Liu X, Woodruff ML, Calvert PD, Savchenko AB, Anderson RE, Fain GL, Li T, Sandberg MA, Dizhoor AM (2006) Effects of low AIPL1 expression on phototransduction in rods. Invest Ophthalmol Vis Sci 47:2185–2194. CrossRef Medline

Mansergh F, Orton NC, Vessey JP, Lalonde MR, Stell WK, Tremblay F, Barnes S, Rancourt DE, Bech-Hansen NT (2005) Mutation of the calcium channel gene Cacna1f disrupts calcium signaling, synaptic transmission and cellular organization in mouse retina. Hum Mol Genet 14:3035–3046. CrossRef Medline

McRory JE, Hamid J, Doering CJ, Garcia E, Parker R, Hamming K, Chen L, Hildebrand M, Beedle AM, Feldcamp L, Zamponi GW, Snutch TP (2004) The CACNA1F gene encodes an L-type calcium channel with unique biophysical properties and tissue distribution. J Neurosci 24:1707–1718. CrossRef Medline

Mennerick S, Zenisek D, Matthews G (1997) Static and dynamic membrane properties of large-terminal bipolar cells from goldfish retina: experimental test of a compartment model. J Neurophysiol 78:51–62. Medline

Michalakis S, Shaltiel L, Sothilingam V, Koch S, Schludi V, Krause S, Zeitz C, Audo I, Lancelot ME, Hamel C, Meunier I, Preising MN, Friedburg C, Lorenz B, Zabouri N, Haverkamp S, Garcia Garrido M, Tanimoto N, Seeliger MW, Biel M, Wahl-Schott CA (2014) Mosaic synaptopathy and functional defects in Cav1.4 heterozygous mice and human carriers of CSNB2. Hum Mol Genet 23:1538–1550. CrossRef Medline

Miki T, Kiyonaka S, Uriu Y, De Waard M, Wakamori M, Beedle AM, Campbell KP, Mori Y (2007) Mutation associated with an autosomal domi-

nant cone-rod dystrophy CORD7 modifies RIM1-mediated modulation of voltage-dependent Ca2+ channels. Channels 1:144–147. CrossRef Medline

Morgans CW (2001) Localization of the alpha(1F) calcium channel subunit in the rat retina. Invest Ophthalmol Vis Sci 42:2414–2418. Medline

Müller M, Liu KS, Sigrist SJ, Davis GW (2012) RIM controls homeostatic plasticity through modulation of the readily-releasable vesicle pool. J Neurosci 32:16574–16585. CrossRef Medline

Neef A, Khimich D, Pirih P, Riedel D, Wolf F, Moser T (2007) Probing the mechanism of exocytosis at the hair cell ribbon synapse. J Neurosci 27: 12933–12944. CrossRef Medline

Nikonov SS, Brown BM, Davis JA, Zuniga FI, Bragin A, Pugh EN Jr, Craft CM (2008) Mouse cones require an arrestin for normal inactivation of phototransduction. Neuron 59:462–474. CrossRef Medline

Olmsted JB (1981) Affinity purification of antibodies from diazotized paper blots of heterogeneous protein samples. J Biol Chem 256:11955–11957. Medline

Picaud SA, Larsson HP, Grant GB, Lecar H, Werblin FS (1995b) Glutamate-gated chloride channel with glutamate-transporter-like properties in cone photoreceptors of the tiger salamander. J Neurophysiol 74:1760–1771. Medline

Picaud S, Larsson HP, Wellis DP, Lecar H, Werblin F (1995a) Cone photoreceptors respond to their own glutamate release in the tiger salamander. Proc Natl Acad Sci U S A 92:9417–9421. CrossRef Medline

Regus-Leidig H, Specht D, Tom Dieck S, Brandstätter JH (2010) Stability of active zone components at the photoreceptor ribbon complex. Mol Vis 16:2690–2700. Medline

Schmitz F (2001) Immunological heterogeneity of synaptic and extrasynaptic forms of non-erythroid alpha-spectrin in the rat retina. Neurosci Lett 313:25–28. CrossRef Medline

Schmitz F, Königstorfer A, Südhof TC (2000) RIBEYE, a component of synaptic ribbons: a protein's journey through evolution provides insight into synaptic ribbon function. Neuron 28:857–872. CrossRef Medline

Schmitz F, Natarajan S, Venkatesan JK, Wahl S, Schwarz K, Grabner CP (2012) EF hand-mediated Ca- and cGMP-signaling in photoreceptor synaptic terminals. Front Mol Neurosci 5:26. Medline

Schoch S, Castillo PE, Jo T, Mukherjee K, Geppert M, Wang Y, Schmitz F, Malenka RC, Südhof TC (2002) RIM1alpha forms a protein scaffold for regulating neurotransmitter release at the active zone. Nature 415:321–326. CrossRef Medline

Schoch S, Mittelstaedt T, Kaeser PS, Padgett D, Feldmann N, Chevaleyre V, Castillo PE, Hammer RE, Han W, Schmitz F, Lin W, Südhof TC (2006) Redundant functions of RIM1alpha and RIM2alpha in Ca(2+)-triggered neurotransmitter release. EMBO J 25:5852–5863. CrossRef Medline

Simms BA, Zamponi GW (2014) Neuronal voltage-gated calcium channels: structure, function, and dysfunction. Neuron 82:24–45. CrossRef Medline

Simms BA, Souza IA, Zamponi GW (2014) Effect of the Brugada syndrome mutation A39V on calmodulin regulation of Cav1.2 channels. Mol Brain 7:34. CrossRef Medline

Specht D, Wu SB, Turner P, Dearden P, Koentgen F, Wolfrum U, Maw M, Brandstätter JH, tom Dieck S (2009) Effects of presynaptic mutations on a postsynaptic Cacna1s calcium channel colocalized with mGluR6 at mouse photoreceptor ribbon synapses. Invest Ophthalmol Vis Sci 50: 505–515. CrossRef Medline

Südhof TC (2012) The presynaptic active zone. Neuron 75:11–25. CrossRef Medline

Szmajda BA, Devries SH (2011) Glutamate spillover between mammalian cone photoreceptors. J Neurosci 31:13431–13441. CrossRef Medline

Tachibana M, Kaneko A (1988) L-glutamate-induced depolarization in solitary photoreceptors: a process that may contribute to the interaction between photoreceptors in situ. Proc Natl Acad Sci U S A 85:5315–5319. CrossRef Medline

Tan GM, Yu D, Wang J, Soong TW (2012) Alternative splicing at C terminus of Ca(V)1.4 calcium channel modulates calcium-dependent inactivation, activation potential, and current density. J Biol Chem 287:832–847. CrossRef Medline

Thoreson WB, Rabl K, Townes-Anderson E, Heidelberger R (2004) A highly Ca2+-sensitive pool of vesicles contributes to linearity at the rod photoreceptor ribbon synapse. Neuron 42:595–605. CrossRef Medline

Toledo D, Ramon E, Aguilà M, Cordomí A, Pérez JJ, Mendes HF, Cheetham ME, Garriga P (2011) Molecular mechanisms of disease for mutations at Gly-90 in rhodopsin. J Biol Chem 286:39993–40001. CrossRef Medline

tom Dieck S, Altrock WD, Kessels MM, Qualmann B, Regus H, Brauner D, Fejtová A, Bracko O, Gundelfinger ED, Brandstatter JH (2005) Molecular dissection of the photoreceptor ribbon synapse: physical interaction of Bassoon and RIBEYE is essential for the assembly of the ribbon complex. J Cell Biol 168:825–836. CrossRef Medline

Tse DY, Chung I, Wu SM (2014) Pharmacological inhibitions of glutamate transporters EAAT1 and EAAT2 compromise glutamate transport in photoreceptor to ON-bipolar cell synapses. Vision Res 103:49–62. CrossRef Medline

Wahl S, Katiyar R, Schmitz F (2013) A local, periactive zone endocytic machinery at photoreceptor synapses in close vicinity to synaptic ribbons. J Neurosci 33:10278–10300. CrossRef Medline

Wan QF, Heidelberger R (2011) Synaptic release at mammalian bipolar cell terminals. Vis Neurosci 28:109–119. CrossRef Medline

Wang Y, Südhof TC (2003) Genomic definition of RIM proteins: evolutionary amplification of a family of synaptic regulatory proteins(small star, filled). Genomics 81:126–137. CrossRef Medline

Wang Y, Okamoto M, Schmitz F, Hofmann K, Südhof TC (1997) Rim is a putative Rab3 effector in regulating synaptic-vesicle fusion. Nature 388: 593–598. CrossRef Medline

Zabouri N, Haverkamp S (2013) Calcium channel-dependent molecular maturation of photoreceptor synapses. PLoS One 8:e63853. CrossRef Medline

Zampighi GA, Schietroma C, Zampighi LM, Woodruff M, Wright EM, Brecha NC (2011) Conical tomography of a ribbon synapse: structural evidence for vesicle fusion. PLoS One 6:e16944. CrossRef Medline

Zampini V, Johnson SL, Franz C, Lawrence ND, Münkner S, Engel J, Knipper M, Magistretti J, Masetto S, Marcotti W (2010) Elementary properties of CaV1.3 Ca(2+) channels expressed in mouse cochlear inner hair cells. J Physiol 588:187–199. CrossRef Medline

Zhang H, Li S, Doan T, Rieke F, Detwiler PB, Frederick JM, Baehr W (2007) Deletion of PrBP/delta impedes transport of GRK1 and PDE6 catalytic subunits to photoreceptor outer segments. Proc Natl Acad Sci U S A 104: 8857–8862. CrossRef Medline